Sparse interferometric Stokes imaging under polarization constraint (Polarized SARA)

Monthly Notices
of the
ROYAL ASTRONOMICAL SOCIETY

MNRAS **478,** 4442–4463 (2018) doi:10.1093/mnras/sty1182

Sparse interferometric Stokes imaging under the polarization constraint (Polarized SARA)

Jasleen Birdi,* Audrey Repetti and Yves Wiaux

Institute of Sensors, Signals and Systems, Heriot-Watt University, Edinburgh EH14 4AS, UK

Accepted 2018 April 25. Received 2018 March 29; in original form 2017 December 31

ABSTRACT

We develop a novel algorithm for sparse imaging of Stokes parameters in radio interferometry under the polarization constraint. The latter is a physical non-linear relation between the Stokes parameters, imposing the polarization intensity as a lower bound on the total intensity. To solve the joint inverse Stokes imaging problem including this bound, we leverage epigraphical projection techniques in convex optimization and we design a primal–dual method offering a highly flexible and parallelizable structure. In addition, we propose to regularize each Stokes parameter map through an average sparsity prior in the context of a reweighted analysis approach (SARA). The resulting method is dubbed Polarized SARA. Using simulated observations of M87 with the Event Horizon Telescope, we demonstrate that imposing the polarization constraint leads to superior image quality. For the considered data sets, the results also indicate better performance of the average sparsity prior in comparison with the widely used Cotton–Schwab CLEAN algorithm and other total variation based priors for polarimetric imaging. Our MATLAB code is available online on GitHub.

Key words: techniques: high angular resolution – techniques: image processing – techniques: interferometric – techniques: polarimetric.

1 INTRODUCTION

The study of the polarized emissions from various astrophysical sources in the Universe provides invaluable information about the origin as well as the medium of propagation of these emissions. In many cases, these sources generate appreciable linearly polarized radiations and only negligible circularly polarized radiations. Thus, the study of linearly polarized emissions is of particular interest. These radiations can be generated, for instance, due to the synchrotron emission from the electrons in high-energy objects (Ginzburg & Syrovatskii 1965). Analysis of these polarized emissions gives insight into the strength and orientation of the magnetic field in the sources. Moreover, while traversing, the interaction with the magnetized plasma along the line of sight to the source can modify the polarization state of these radiations via processes such as Faraday rotation (Pacholczyk 1970; Simard-Normandin, Kronberg & Button 1981). As a result, the polarized emissions also characterize the magnetic field distributions of these plasmas (Dreher, Carilli & Perley 1987; Brentjens & De Bruyn 2005). This all indicates the importance of imaging these polarized emissions, which is referred to as polarimetric imaging.

In the context of polarimetric imaging for radio interferometry (RI), the intensity distribution of the sky image of interest is characterized by the Stokes parameters, I, Q, U and V, which are all real valued. While I represents the total intensity of the radio emissions, Q, U and V describe the polarization state of the electromagnetic radiations coming from the target area of the sky. In particular, Q and U refer to the linear polarization, and V denotes the circular polarization. Furthermore, the linear polarization image P is given by $P = Q + \mathrm{i}\,U$. The magnitude of this complex valued quantity provides the linear polarization intensity, while the electric vector polarization angle (EVPA) can be obtained from its phase. Importantly, the Stokes parameters are not completely independent but are constrained by a physical non-linear relation imposing that the polarization intensity is a lower bound on the total intensity: $\sqrt{Q^2 + U^2 + V^2} \leq I$. We can also see this constraint, namely the polarization constraint, as the generalization of the more simple positivity constraint on the intensity image in the context of unpolarized imaging.

In order to produce linear polarimetric images at very high angular resolutions, one of the possibilities is to leverage the technique of very long baseline interferometry (VLBI; Roberts, Wardle & Brown 1994). VLBI consists of a collection of radio antennas, spread all across the Earth or even in space (space VLBI), with the aim of producing images of the target sources in the sky at very high angular resolutions. Very recently, the Event Horizon Tele-

* E-mail: jb36@hw.ac.uk

scope (EHT)[1], a ground-based VLBI array, has been designed to observe the immediate environment around a black hole at angular resolutions comparable to the event horizon. The primary observing targets of the EHT are the supermassive black hole Sgr A* at the centre of the Milky Way galaxy (Doeleman et al. 2008), and the nucleus of M87, a giant elliptical galaxy in the constellation Virgo (Doeleman et al. 2012; Akiyama et al. 2015). In view of the discussion above, polarimetric imaging with the EHT data can yield extremely valuable information about the magnetic field distribution and magnetized plasma in the regions around these targets. However, the radio interferometers do not directly provide an image as an output. Indeed, the interferometric measurements consist of complex visibilities that are related to the Fourier transform of the brightness distribution of the sky image of interest (Thompson, Moran & Swenson 2001). As each such visibility is acquired by a pair of antennas in the interferometer and the number of antennas are limited, a sparse sampling of the Fourier plane is observed. Although this Fourier coverage is enhanced by making use of the Earth's rotation, the resultant coverage is still incomplete. This leads to a highly underdetermined problem of RI image reconstruction. There are a number of methods in the literature to solve the corresponding problem. All these methods were initially developed for the Stokes *I* imaging only. Later, some of these methods were extended to polarimetric imaging. In this context, the most widely used algorithm is CLEAN (Högbom 1974). It implements a greedy, non-linear iterative deconvolution approach. With regards to polarimetric imaging, CLEAN solves for each of the Stokes images in the same manner, although totally independently. Basically, given the Stokes visibilities corresponding to any of the Stokes parameters, each iteration involves the computation of the residual dirty image wherein the maximum intensity pixel is searched for. This is followed by a beam removal step where, based on a loop gain factor, a fraction of this pixel's value convolved with the dirty beam is removed. The process is continued until the maximum intensity value in the dirty image becomes lower than some threshold value. Working pixel by pixel, CLEAN implicitly considers the sought image to be sparse. Many variants of CLEAN have also been proposed these last years, notably its multi-scale (Cornwell 2008) and adaptive scale (Bhatnagar & Cornwell 2004) versions. It is worth mentioning that, in essence, CLEAN has been shown to be very similar to some of the existing optimization algorithms in the literature. In particular, it shares many attributes with the matching pursuit algorithm (Mallat & Zhang 1993). Lately, the analogies of CLEAN with a sparsity regularized gradient descent method have been shown in Rau et al. (2009), Carrillo, McEwen & Wiaux (2014) and Onose et al. (2016). Another technique called Generalized Complex CLEAN has been proposed by Pratley & Johnston-Hollitt (2016) for polarimetric imaging. This technique is basically a modification of the CLEAN algorithm. Unlike CLEANing independently for the real-valued Stokes *Q* and *U* images, as done in the traditional CLEAN methods, Pratley & Johnston-Hollitt (2016) propose to CLEAN the complex-valued linear polarization image *P*. This offers the advantage of rotational invariance and detection of more true components in sources near the noise level.

In recent years, there has been a lot of interest in techniques based on compressive sensing (CS). In the context of RI imaging, these techniques were pioneered by Wiaux et al. (2009), followed by other works including Wiaux, Puy & Vandergheynst (2010), Li, Cornwell & De hoog (2011), Carrillo, McEwen & Wiaux (2012), Carrillo et al. (2014), Garsden et al. (2015) and Onose et al. (2016), to name a few. In particular, these techniques reconstruct the image of interest by leveraging the sparsity of the sought image, either in the image domain or in a transformed domain. Though applied only for Stokes *I* image reconstruction, the quality of reconstruction obtained by these techniques has been shown to outperform that obtained by CLEAN on simulated as well as on a few real data sets (Carrillo, McEwen & Wiaux 2014; Onose et al. 2016; Pratley et al. 2016; Onose, Dabbech & Wiaux 2017; Dabbech et al. 2017a). Very recently, the first application of these sparsity regularized methods for polarimetric imaging has been developed by Akiyama et al. (2017a). In this case, the authors promote the sparsity of the underlying images using the ℓ_1 norm along with the total variation (TV) regularization (Rudin, Osher & Fatemi 1992; Chambolle & Lions 1997), and they solve the resultant problem using a monotonic version of fast iterative shrinkage/thresholding algorithm (FISTA; Beck & Teboulle 2009a,b). The authors validate their technique on simulated EHT data and obtain super-resolved Stokes images. The resolution of the reconstructed images is much higher than that obtained by CLEAN. However, similar to CLEAN, this sparsity-based approach also solves independently for the Stokes images.

In practice, the Stokes images are physically linked. As previously discussed, due to the polarization constraint, the intensity in each pixel of the total intensity image cannot be smaller than the corresponding polarization intensity. Nevertheless, to the best of our knowledge, none of the previously mentioned methods takes this constraint explicitly into account. It is worth mentioning then that in the absence of this constraint, non-physical reconstructions may be produced. One way to reconstruct the images with physical meaning is to make use of maximum entropy methods (MEMs). These methods aim to find an image that maximizes the entropy function while being consistent with the acquired data (Cornwell & Evans 1985). As an extension to polarimetric MEM, a special entropy function incorporating this polarization constraint is used (Narayan & Nityananda 1986; Holdaway & Wardle 1990; Coughlan & Gabuzda 2016; Chael et al. 2016). Another means to impose the polarization constraint is by employing the strategy of the change of variables. This consists of representing the polarimetric images in terms of their fractional polarization and position angle, and solving directly for these variables (Chael et al. 2016). However, adopting this approach amounts to solving a non-convex optimization problem, which may not benefit from convergence guarantees to the global minimum.

In this paper, we propose a new CS-based method for joint estimation of Stokes images. More specifically, we develop a sparse imaging method that jointly solves for the Stokes parameter maps under the polarization constraint. Our contribution is twofold. First, within the proposed sparse modelling framework, the novelty of our method lies in taking into account the polarization constraint explicitly in the image reconstruction problem. Difficult to be handled by the classical optimization approaches while keeping the underlying minimization problem convex, we propose to enforce this constraint by employing the technique of epigraphical projections. The latter consists in splitting the associated constraint set into easily manageable sets through simple projections (Chierchia et al. 2015). Secondly, we generalize to polarimetric imaging the sparsity averaging reweighted analysis (SARA) approach introduced for Stokes *I* imaging in Carrillo et al. (2013, 2014). The resultant approach, referred to as Polarized SARA, now promotes average sparsity of each of the Stokes images *I*, *Q*, *U* and *V*. While the original SARA for intensity imaging also imposes positivity of the Stokes *I* map,

[1] http://eventhorizontelescope.org

Polarized SARA accounts for the polarization constraint for joint Stokes imaging. In order to solve the corresponding image reconstruction problem, we develop an iterative algorithm based on a primal–dual method (Combettes & Pesquet 2011; Condat 2013; Vũ 2013; Pesquet & Repetti 2015). It is important to emphasize that, even if the method is described in the context of sparsity averaging regularization, the proposed algorithm can be used for any other prior.

Although sparse modelling techniques have already been applied for polarimetric imaging by Akiyama et al. (2017a) using ℓ_1 and TV-based regularizations, as pointed out earlier, they do not consider a joint imaging problem. They instead solve independently for each of the Stokes parameters, without imposing the polarization constraint. It is worth noting that their imaging problem can be solved using a similar primal–dual based approach, as the one developed in this article. Indeed, Akiyama et al. (2017a) employ monotonic FISTA to solve their problem, which involves sub-iterations to compute the proximity operator for the ℓ_1 + TV term (Beck & Teboulle 2009a). In contrast, the proposed primal–dual approach can deal with this term (in general, for the sum of any number of such priors) without requiring any such sub-iterations (Chambolle & Pock 2010; Komodakis & Pesquet 2015). For the sake of completeness, we also propose to introduce the polarization constraint in their image reconstruction problem, and to solve the resulting problem using epigraphical projections in a primal–dual framework.

The outline of the paper is as follows. In Section 2, we lay the foundations for our work. In particular, we describe the RI imaging model for full polarization and we pose the inverse problem for polarimetric imaging. In Section 3, we discuss the CS and the optimization frameworks, which are then used to design our polarimetric method. We give a detailed description of the proposed approach in Section 4. We then investigate the performance of the proposed algorithm on simulated EHT data in Section 5. We conclude in Section 6 and discuss future work.

2 FULL POLARIZATION OBSERVATION MODEL

2.1 Problem description

A radio interferometer comprises an array of antennas, designed to image the radio sources in a given sky area. In order to image the Stokes parameters, each antenna pair in the interferometer provides a set of measurements, called the visibilities, at time instants $t \in \{1, \ldots, T\}$. For a better understanding, let us consider an interferometer consisting of N_a antennas, such that each antenna pair is labelled by $(\alpha, \beta) \in \{1, \ldots, N_\mathrm{a}\}^2$, with $\alpha < \beta$. Furthermore, referring to the separation between each antenna pair by the term baseline, let the baseline components corresponding to an antenna pair (α, β) at time t be denoted by $(u_{\alpha,\beta,t}, v_{\alpha,\beta,t}, w_{\alpha,\beta,t})$, expressed in units of the observation wavelength. While $\boldsymbol{u}_{\alpha,\beta,t} = (u_{\alpha,\beta,t}, v_{\alpha,\beta,t})$ describes the components in the plane perpendicular to the line of sight, $w_{\alpha,\beta,t}$ refers to the component in the line of sight. The Stokes parameters of the target sky image can be expressed by the components $\boldsymbol{l} = (l, m)$ in the plane tangent to the celestial sphere, and by the component $n(\boldsymbol{l}) = \sqrt{1 - l^2 - m^2}$ in the line of sight, with $l^2 + m^2 \leq 1$. The target sky intensity distribution can vary with the observation time and frequency. In this context, for each time instant t and observation frequency ν, the radio interferometric measurement equation (RIME) is given by (Smirnov 2011)

$$\boldsymbol{y}^{\top}_{\alpha,\beta,t,\nu} = \int \boldsymbol{S}^{\top}_{t,\nu}(\boldsymbol{l})\, \mathbf{L}\, \mathbf{D}^{\top}_{\alpha,\beta,t,\nu}(\boldsymbol{l})\, \mathrm{e}^{-\mathrm{i}2\pi \boldsymbol{u}_{\alpha,\beta,t}\cdot \boldsymbol{l}}\, \mathrm{d}^2\boldsymbol{l}, \tag{1}$$

where $(.)^{\top}$ denotes the transpose operation of its argument. In equation (1), $\boldsymbol{y}_{\alpha,\beta,t,\nu} \in \mathbb{C}^4$ is the full polarization visibility vector corresponding to the measurements made by the antenna pair (α, β) at time instant t and observation frequency ν. It can be seen as the Fourier transform of the product of brightness distribution and the Mueller matrix, at the spatial frequency $\boldsymbol{u}_{\alpha,\beta,t}$ (Hamaker, Bregman & Sault 1996; Thompson et al. 2001; Rau et al. 2009). More specifically, $\mathbf{L}$ denotes the linear operator that acts on the Stokes vector $\boldsymbol{S}^{\top}_{t,\nu}(\boldsymbol{l}) = [I,\ Q,\ U,\ V]_{t,\nu}(\boldsymbol{l})$ to give the brightness vector. In practice, it is defined depending on the choice of the antenna feeds under consideration (i.e. whether circular or linear; see Hamaker et al. 1996; Smirnov 2011). For instance, in the case of the EHT, which uses circular feeds, the brightness vector is given as

$$\boldsymbol{S}^{\top}_{t,\nu}(\boldsymbol{l})\mathbf{L} = [I + V,\ Q + \mathrm{i}U,\ Q - \mathrm{i}U,\ I - V]_{t,\nu}(\boldsymbol{l}). \tag{2}$$

It should be mentioned here that instead of applying the inverse of the operator $\mathbf{L}$ on the measured data vector, we consider $\mathbf{L}$ acting on $\boldsymbol{S}^{\top}_{t,\nu}(\boldsymbol{l})$ in the measurement model to avoid introducing correlated thermal noise among the different measurements.

The 4×4 Mueller matrix $\mathbf{D}_{\alpha,\beta,t,\nu}(\boldsymbol{l})$ is obtained from the Kronecker product of 2×2 Jones matrices defined for antennas α and β at time t and frequency ν (Hamaker et al. 1996). The Mueller matrix for each antenna pair is generally dependent on the angular position $\boldsymbol{l}$ on the sky to incorporate not only the direction-independent effects (DIEs) but also the direction-dependent effects (DDEs). These effects are either known (e.g. the w component; Cornwell, Golap & Bhatnagar 2008; Offringa et al. 2014; Dabbech et al. 2017b) or need to be calibrated (Smirnov 2011; Salvini & Wijnholds 2014; Smirnov & Tasse 2015; Van Weeren et al. 2016; Repetti et al. 2017; Sokolowski et al. 2017). The Mueller matrices can also have non-zero off-diagonal components, corresponding to the cross-polarization leakage. Therefore, each component of the visibility vector $\boldsymbol{y}_{\alpha,\beta,t,\nu}$ gathers contributions from all the Stokes parameters.

For the sake of our considerations, we restrict our settings to the brightness distributions with neither time nor frequency dependency, with a single observation frequency. This implies that $\boldsymbol{S}_{t,\nu}(\boldsymbol{l}) = \boldsymbol{S}(\boldsymbol{l})$, and the frequency index is dropped for all other variables for ease of notation.

In order to recover the Stokes images from the given measurements, we consider a discretized version of the inverse problem in equation (1). To this aim, we denote the Stokes matrix by $\overline{\mathbf{S}} = [\bar{s}_1, \bar{s}_2, \bar{s}_3, \bar{s}_4] \in \mathbb{R}^{N\times 4}$, which corresponds to the concatenation of the discretized Stokes maps. In this context, $\bar{s}_1, \bar{s}_2, \bar{s}_3$ and $\bar{s}_4$, each belonging to $\mathbb{R}^N$, denote the discretization of the Stokes images I, Q, U and V, respectively. In accordance with equation (1), we denote the measurement matrix by $\mathbf{Y} \in \mathbb{C}^{M\times 4}$, where each row $m \in \{1, \ldots, M\}$ corresponds to the full polarization measurements acquired by a given antenna pair (α, β) at time t. With these definitions in mind, the discretized measurement model is given by

$$\mathbf{Y} = \Phi(\overline{\mathbf{S}}) + \mathbf{E}, \tag{3}$$

where the measurements are corrupted by a random additive noise, represented by the matrix $\mathbf{E} \in \mathbb{C}^{M\times 4}$. Each column of the matrix $\mathbf{E}$ is a realization of such an additive Gaussian noise. The measurement operator $\Phi : \mathbb{C}^{N\times 4} \to \mathbb{C}^{M\times 4}$ in equation (3) acts on the Stokes matrix to give the measurements $\mathbf{Y}$. In particular, at each

observation instant t and within the considered discrete setting, it consists of computing the Fourier transform of the multiplication of the Mueller matrix $\mathbf{D}_{\alpha,\beta,t}$ with the brightness matrix $\overline{\mathbf{S}}\mathbf{L}$, at the sampled frequencies $\boldsymbol{u}_{\alpha,\beta,t}$ for all the antenna pairs. It should be mentioned here that calibrating for the DIEs and DDEs is out of the scope of the current paper wherein the operator Φ is assumed to be known beforehand.

2.2 Polarization constraint

One of the key contributions of the current work is exploiting the polarization constraint for the estimation of the Stokes images by solving problem (3). This constraint, as discussed in Section 1, physically links the Stokes images, and is defined as

$$\forall n \in \{1, \ldots, N\}, \quad -\mathbf{S}_{n,1} + \|\mathbf{S}_{n,2:4}\|_2 \leq 0, \tag{4}$$

where, for every $n \in \{1, \ldots, N\}$, $\mathbf{S}_{n,1}$ denotes the nth coefficient of the first column of the matrix $\mathbf{S}$, and the notation $\mathbf{S}_{n,2:4}$ signifies the nth coefficients of columns 2–4 of the matrix (50). In order to enforce this constraint within a convex, sparse modelling framework, we develop a new method, which we describe later.

$$\mathbf{S} \tag{50}$$

3 COMPRESSIVE SENSING AND OPTIMIZATION

3.1 Compressive sensing framework

In recent years, the CS framework has gained a lot of attention in the research community (Candès, Romberg & Tao 2006; Donoho 2006). It often employs convex optimization methods to solve ill-posed inverse problems, exploiting the sparsity of the sought image. In the context of RI imaging, this framework has been introduced in Wiaux et al. (2009). Since then, as mentioned in Section 1, CS based techniques have been extensively applied for Stokes I imaging providing better reconstruction quality than that obtained by the standard CLEAN algorithm (Carrillo et al. 2014; Onose et al. 2016, 2017; Pratley et al. 2016; Dabbech et al. 2017a). However, it is worth mentioning that reducing the computational cost of these optimization based methods is still an area of ongoing investigation.

Generally, inverse problems of the form of equation (3) are ill-posed or ill-conditioned. Indeed, as described in Section 2, the measurements only contain partial information of the image of interest, often corrupted by additive noise. Then, solving problem (3) is a challenging task, and a suitable approach needs to be adapted. To overcome this difficulty, the CS theory assumes that the target signal has a sparse representation in a dictionary. More specifically, given a sparsifying dictionary $\boldsymbol{\Psi} \in \mathbb{C}^{N \times J}$, the sparse representation of the signal $\overline{\mathbf{S}}$ in this dictionary is given by $\boldsymbol{\Psi}^\dagger \overline{\mathbf{S}}$, where $\boldsymbol{\Psi}^\dagger$ is the adjoint operator of $\boldsymbol{\Psi}$. The first task is to choose an appropriate dictionary for the image under consideration. In this context, many studies have been performed in the past (Rubinstein, Bruckstein & Elad 2010; Starck, Murtagh & Fadili 2010). These studies indicate that for the simplest case of considering an already sparse image (i.e. an image consisting of point sources), $\boldsymbol{\Psi}$ can be chosen to be the Dirac basis (i.e. identity matrix with $J = N$), promoting sparsity in the image domain itself. However, when the underlying images are smooth and have more complex structures, the possibilities of this sparsifying dictionary $\boldsymbol{\Psi}$ include the wavelet domain (Mallat 2009), or a collection of wavelet bases (Carrillo et al. 2012). Furthermore, in the case of piece-wise constant images, the gradient domain is usually the best option for promoting sparsity, using total variation based regularizations (Rudin et al. 1992; Wiaux et al. 2010). Once a suitable dictionary is chosen, within the CS framework, the next task is to solve the underlying inverse problem by promoting the sparsity of the sought image in the domain determined by the chosen dictionary.

The best way to promote sparsity of a variable is to use the ℓ_0 pseudo norm (Donoho et al. 1995). The ℓ_0 pseudo norm of any signal is defined to be the number of its non-zero components. Therefore, by definition, minimizing this norm eventually leads to reduction in the number of non-zero elements, thereby promoting sparsity of the given signal. However, because of its non-convexity, solving the problem for the ℓ_0 norm is often intractable, especially for large dimensional problems. Instead, its convex relaxation (i.e. the ℓ_1 norm) is often considered (Chen, Donoho & Saunders 2001). A probable drawback of the ℓ_1 norm as a sparsity-inducing term is its dependence on the magnitude of the signal coefficients. To mimic the behaviour of the ℓ_0 pseudo norm more appropriately, this dependence can be alleviated by the use of the weighted ℓ_1 norm. For any matrix $\mathbf{S} \in \mathbb{R}^{N \times 4}$, its weighted ℓ_1 norm is defined as

$$\|\boldsymbol{\Psi}^\dagger \mathbf{S}\|_{\mathbf{W},1} = \sum_{i=1}^{4} \sum_{j=1}^{J} \mathbf{W}_{j,i} \left| [\boldsymbol{\Psi}^\dagger \mathbf{S}]_{j,i} \right|, \tag{5}$$

where the notation $[.]_{j,i}$ stands for the coefficient in the jth row and ith column of the argument matrix. Additionally, $\mathbf{W} \in \mathbb{R}_+^{J \times 4}$ is the weighting matrix such that each column comprises the weights for the signal in the corresponding column of the matrix $\mathbf{S}$. With this approach, the estimate of the signal $\overline{\mathbf{S}}$ from the degraded measurements $\mathbf{Y}$ is defined to be a solution of the following minimization problem

$$\underset{\mathbf{S} \in \mathbb{R}^{N \times 4}}{\text{minimize}} \ \|\boldsymbol{\Psi}^\dagger \mathbf{S}\|_{\mathbf{W},1} \ \text{ subject to } \ \|\mathbf{Y} - \Phi(\mathbf{S})\|_2 \leq \epsilon, \tag{6}$$

where $\epsilon > 0$ is an upper bound on the norm of the additive noise, and for any matrix $\mathbf{X}$, the term $\|\mathbf{X}\|_2$ denotes its Frobenious norm. Moreover, the Lagrangian function associated with problem (6) provides its unconstrained formulation, given by

$$\underset{\mathbf{S} \in \mathbb{R}^{N \times 4}}{\text{minimize}} \ \mu \|\boldsymbol{\Psi}^\dagger \mathbf{S}\|_{\mathbf{W},1} + \frac{1}{2} \|\mathbf{Y} - \Phi(\mathbf{S})\|_2^2, \tag{7}$$

where $\mu > 0$. Many efficient convex optimization techniques, discussed in the next section, can be used to solve the resultant minimization problem, whether it is the constrained (6) or unconstrained (7) formulation. In this context, while in problem (7) the parameter μ needs to be tuned, problem (6) requires the value of ϵ to be specified, which can be theoretically determined when the noise statistics and the measurement operator are known accurately (Carrillo et al. 2012; Onose et al. 2016). In practice, the presence of the calibration errors leads to mismodelling of the measurement operator, thereby affecting the ℓ_2 bound ϵ in problem (6). In such a case with unknown errors, the value of ϵ can be estimated using an adaptive scheme proposed in Dabbech et al. (2017a). Thus, especially for cases with complex visibility measurements, problem (6) is often preferred over problem (7).

Regarding the choice of the weights, these should be such that the small valued coefficients are penalized. To determine these weights, Candès, Wakin & Boyd (2008) proposed to solve iteratively a sequence of the weighted ℓ_1 minimization problems – either problem (6) or (7) – referred to as the reweighting scheme. By doing so, the weights at each iteration are computed by taking the inverse of the solution from the previous iteration. In the

context of radio interferometric imaging, the effectiveness of this scheme has been demonstrated in Carrillo et al. (2012) and Onose et al. (2017).

3.2 Optimization framework

In order to solve the inverse problem (3) using the CS framework described above, we resort to convex optimization techniques. In particular, in this work we develop an iterative algorithm based on proximal splitting methods. The main advantages of these methods are their flexibility to deal with very sophisticated minimization problems, and their scalability offering the possibility to handle large dimensional variables. An overview of these methods has been provided in Combettes & Pesquet (2011) and Komodakis & Pesquet (2015). They can be employed to solve a wide class of problems which can be expressed in the following form

$$\underset{\mathbf{S}\in\mathbb{R}^{N\times 4}}{\text{minimize}} \sum_{k=1}^{K} f_k(\mathbf{S}), \tag{8}$$

where for $k \in \{1, \ldots, K\}$, f_k is a proper, lower-semicontinuous convex function from $\mathbb{R}^{N\times 4}$ to $]-\infty, +\infty]$. It is important to emphasize that problem (8) is very general and that most of the problems encountered in signal and image processing applications can be written using this formulation. Indeed any constrained problem can be reformulated as equation (8). This can be achieved by casting one of the functions f_k as an indicator function of the constraint set of interest. Let $\mathcal{C} \subset \mathbb{R}^{N\times 4}$ represent such a non-empty closed convex set. Then, the indicator function of this set, at a given point $\mathbf{S} \in \mathbb{R}^{N\times 4}$, is defined as

$$\iota_{\mathcal{C}}(\mathbf{S}) = \begin{cases} 0, & \text{if } \mathbf{S} \in \mathcal{C}, \\ +\infty, & \text{otherwise.} \end{cases}$$

Another interesting point of problem (8) is that it can take into account both smooth and non-smooth functions. In practice, to handle these functions, proximal splitting methods will use the gradients of the smooth functions and the proximity operators of the non-smooth functions. Formally, the proximity operator of a function $f : \mathbb{R}^{N\times 4} \to]-\infty, +\infty]$ at the point $\mathbf{S}$ is defined as

$$\text{prox}_f(\mathbf{S}) = \underset{\mathbf{U}\in\mathbb{R}^{N\times 4}}{\text{argmin}}\ f(\mathbf{U}) + \frac{1}{2}\|\mathbf{U}-\mathbf{S}\|_2^2. \tag{9}$$

This operator can be seen as a generalization of the projection operator $\mathcal{P}_{\mathcal{C}}$ on to the set $\mathcal{C} \subset \mathbb{R}^{N\times 4}$, i.e.

$$\mathcal{P}_{\mathcal{C}}(\mathbf{S}) = \underset{\mathbf{U}\in\mathcal{C}}{\text{argmin}} \|\mathbf{U}-\mathbf{S}\|_2^2 . \tag{10}$$

Based on the proximal splitting methods, problems of the form (8) can be efficiently solved by several existing algorithms, such as the forward–backward algorithm, also known as the iterative soft thresholding algorithm (ISTA; Chen & Rockafellar 1997; Tseng 2000), the Douglas–Rachford algorithm (Eckstein & Bertsekas 1992), etc.

In the particular yet common case of composite problems where the non-smooth functions are composed with a linear operator, adapted methods need to be designed. For instance, consider the following problem

$$\underset{\mathbf{S}\in\mathbb{R}^{N\times 4}}{\text{minimize}}\ f_1(\mathbf{S}) + f_2(\mathbf{TS}), \tag{11}$$

where $f_1 : \mathbb{R}^{N\times 4} \to]-\infty, +\infty]$ is a convex differentiable function, $f_2 : \mathbb{R}^{Q\times 4} \to]-\infty, +\infty]$ is a non-smooth, proper, lower-semicontinuous convex function, and $\mathbf{T} \in \mathbb{R}^{Q\times N}$ is a linear operator. One possibility to solve this problem is by using the forward–backward algorithm, alternating between a gradient step on f_1 and a proximity step on $f_2 \circ \mathbf{T}$. However, use of this approach may require the inversion of the operator $\mathbf{T}$ or performing sub-iterations to compute the proximity step. This can be problematic especially when the dimension of the underlying problem increases. To overcome this issue, recently several primal–dual methods have been proposed (Chambolle & Pock 2010; Combettes & Pesquet 2011; Condat 2013; Vũ 2013; Combettes et al. 2014; Komodakis & Pesquet 2015). Basically, they provide full splitting and solve simultaneously for primal and dual problems. More formally, the dual problem associated with the primal problem (11) is given by

$$\underset{\mathbf{V}\in\mathbb{R}^{Q\times 4}}{\text{minimize}}\ f_1^*(-\mathbf{T}^\dagger\mathbf{V}) + f_2^*(\mathbf{V}), \tag{12}$$

where f_1^* (resp. f_2^*) is the Legendre–Fenchel conjugate function of f_1 (resp. f_2) (Bauschke & Combettes 2011), and $\mathbf{T}^\dagger$ is the adjoint operator of $\mathbf{T}$. Concerning the splitting in the primal–dual methods, it is achieved over all the functions involved in the minimization problem, including the gradient and proximity operators as well as the involved linear operator, thereby preventing the need to invert the linear operator. Thus, these methods offer computational advantages over other splitting methods.

4 POLARIZED SARA

4.1 Objective function for polarimetric imaging

The estimation of the Stokes images from the degraded measurements consists of solving the inverse problem (3). Given its ill-posedness, ensuring the data fidelity is not sufficient to recover the sought images. Indeed, following the CS theory described in Section 3.1, the problem needs to be regularized and a priori information needs to be injected in the reconstruction process. We thus aim to solve a minimization problem consisting of a data fidelity term and a regularization term. The data fidelity term given by

$$f\big(\Phi(\mathbf{S})\big) = \iota_{\mathbb{B}(\mathbf{Y},\epsilon)}\big(\Phi(\mathbf{S})\big) \quad \text{with } \mathbb{B}(\mathbf{Y},\epsilon) = \{\Phi(\mathbf{S}) \in \mathbb{C}^{M\times 4} : \|\Phi(\mathbf{S})-\mathbf{Y}\|_2 \le \epsilon\}, \tag{13}$$

constraints the residual to lie within an ℓ_2 ball centred in $\mathbf{Y}$ and whose radius is determined by the noise level ϵ.

Concerning the regularization term, we use a hybrid function taking into account the following prior information.

Real-valuedness. The Stokes images should be real-valued. This condition can be enforced by the use of an indicator function of a set $\mathbb{U} = \mathbb{R}^{N\times 4}$.

Sparsifying regularization. Leveraging the CS theory, we promote sparsity of the Stokes images in a sparsifying dictionary $\mathbf{\Psi}$. In this context, as discussed in Section 3.1, adopting the reweighting scheme, which consists of iteratively solving the problems with weighted ℓ_1 norm, provides a better estimation of the sought images in the ℓ_0 sense as compared to ℓ_1 norm. Therefore, we propose to use the weighted ℓ_1 norm as the sparsifying regularization term

$$g(\mathbf{\Psi}^\dagger\mathbf{S}) = \|\mathbf{\Psi}^\dagger\mathbf{S}\|_{\mathbf{W},1}. \tag{14}$$

It should be emphasized here that using the weighted ℓ_1 norm also offers the advantage of no tuning of regularization parameters, unlike the case of the ℓ_1 norm. More precisely, as Stokes Q, U and V images are lower in intensity than Stokes I, the latter dominates in the ℓ_1 norm sparsity inducing term. To overcome this unequal contribution of the Stokes images, different regularization parameters need to be chosen for each image. However, because of the

weights in equation (14), all the Stokes images are normalized, and thereby have equal importance in this sparsity term, avoiding the need to use any additional parameters to enhance the contribution of the Stokes Q, U and V images.

It should be mentioned here that any linear sparsifying operator could be used in the proposed method. However, inspired by the sparsity averaging proposed in Carrillo et al. (2013, 2014) for Stokes I imaging, we extend it to polarimetric imaging and choose to promote sparsity averaging for each of the Stokes parameter maps I, Q, U and V. This consists of choosing $\boldsymbol{\Psi}$ as the concatenation of the first eight Daubechies wavelets and Dirac basis (see e.g. Mallat 2009; Onose et al. 2016). Use of this dictionary coupled with the reweighting scheme corresponds to the SARA regularization.

Polarization constraint. We exploit the physical link between the Stokes images by enforcing the polarization constraint, described earlier in Section 2.2. Let $\mathbb{P}$ be the associated polarization constraint set, defined as

$$\mathbb{P} = \left\{ \mathbf{S} \in \mathbb{R}^{N\times 4} \,\middle|\, \left(\forall n \in \{1,\ldots,N\}\right) - \mathsf{S}_{n,1} + \|\mathbf{S}_{n,2:4}\|_2 \leq 0 \right\}. \quad (15)$$

Then, the polarization constraint can be imposed by the use of an indicator function of the set $\mathbb{P}$. Additionally, this constraint can be expressed as $\mathsf{S}_{n,1} \geq \|\mathbf{S}_{n,2:4}\|_2$, where $n \in \{1,\ldots,N\}$. It can then be noticed that it imposes the polarization intensity as a lower bound on the total intensity image, and thus implicitly enforces the positivity of the total intensity image (Stokes I).

With the above-mentioned prior information at hand, our resultant minimization problem to be solved for the Stokes images is given by

$$\underset{\mathbf{S}\in\mathbb{R}^{N\times 4}}{\text{minimize}}\; f\left(\Phi(\mathbf{S})\right) + \iota_{\mathbb{U}}(\mathbf{S}) + g(\boldsymbol{\Psi}^\dagger \mathbf{S}) + \iota_{\mathbb{P}}(\mathbf{S}). \quad (16)$$

It can be observed that enforcing the polarization constraint in problem (16) involves projecting the variable $\mathbf{S}$ on to the set $\mathbb{P}$. However, the associated projection does not have a closed form. Therefore, to impose this constraint, we employ a splitting technique based on epigraphical projection (Chierchia et al. 2015). The epigraphical projection is a recently proposed technique used to handle minimization problems involving sophisticated constraints (see e.g. Harizanov, Pesquet & Steidl 2013; Chierchia et al. 2014; Moerkotte et al. 2015; El-Gheche, Chierchia & Pesquet 2016).

In the case when the polarization constraint is not taken into account, the positivity of the total intensity image is no longer ensured and it needs to be imposed explicitly. This can be done by modifying the set $\mathbb{U}$ to a set $\mathbb{U}'$ given by

$$\mathbb{U}' = \left\{ \mathbf{S} \,\middle|\, \mathbf{S}_{:,1} \in \mathbb{R}^N_+,\ \mathbf{S}_{:,2:4} \in \mathbb{R}^{N\times 3} \right\}. \quad (17)$$

In such a case, problem (16) simplifies to

$$\underset{\mathbf{S}\in\mathbb{R}^{N\times 4}}{\text{minimize}}\; f\left(\Phi(\mathbf{S})\right) + \iota_{\mathbb{U}'}(\mathbf{S}) + g(\boldsymbol{\Psi}^\dagger \mathbf{S}). \quad (18)$$

4.2 Epigraphical projection

The requirement to satisfy the polarization constraint is that the Stokes matrix should belong to the set $\mathbb{P}$. In order to impose this constraint, we utilize the epigraphical projection techniques recently developed by Chierchia et al. (2015). Leveraging these techniques, we propose to introduce an auxiliary variable $\mathbf{Z} \in \mathbb{R}^{N\times 2}$ in the minimization problem (16) and thereby splitting the polarization constraint set into simpler constraint sets, such that the projection on to these sets can be efficiently computed. Doing so, problem (16) can be equivalently rewritten as

$$\underset{\mathbf{S}\in\mathbb{R}^{N\times 4},\mathbf{Z}\in\mathbb{R}^{N\times 2}}{\text{minimize}}\; f\left(\Phi(\mathbf{S})\right) + \iota_{\mathbb{U}}(\mathbf{S}) + g(\boldsymbol{\Psi}^\dagger \mathbf{S}) \quad (19)$$

subject to $(\forall n \in \{1,\ldots,N\})$

$$\begin{cases} h_1(\mathsf{S}_{n,1}) \leq \mathsf{Z}_{n,1}, & (19a)\\ h_2(\mathbf{S}_{n,2:4}) \leq \mathsf{Z}_{n,2}, & (19b)\\ \mathsf{Z}_{n,1} + \mathsf{Z}_{n,2} \leq 0, & (19c) \end{cases}$$

where the functions h_1 and h_2 are defined as

$$(\forall \zeta \in \mathbb{R}) \quad h_1(\zeta) = -\zeta, \quad (20)$$

$$\left(\forall (\boldsymbol{\zeta}) \in \mathbb{R}^3\right) \quad h_2(\boldsymbol{\zeta}) = \|\boldsymbol{\zeta}\|_2. \quad (21)$$

To understand the above-mentioned modified minimization problem, we can observe that the polarization constraint set $\mathbb{P}$, defined in equation (15), can be equivalently rewritten as

$$\mathbb{P} = \left\{ \mathbf{S} \in \mathbb{R}^{N\times 4} \,\middle|\, \left(\forall n \in \{1,\ldots,N\}\right) \right. \\ \left. h_1(\mathsf{S}_{n,1}) + h_2(\mathbf{S}_{n,2:4}) \leq 0 \right\}. \quad (22)$$

Therefore, the Stokes matrix $\mathbf{S}$ satisfying the constraint defined by set $\mathbb{P}$ is equivalent to having the variables $(\mathbf{S}, \mathbf{Z})$ satisfying the constraints defined by equations (19a)–(19c).

To simplify the notation of the minimization problem (19), we need to introduce the definition of the epigraph of a proper, lower semicontinuous function $\psi : \mathbb{R}^N \to]-\infty, +\infty]$. It corresponds to the set of points lying on or above the graph of ψ, and formally, it is given by (Rockafellar & Wets 1997):

$$\operatorname{epi}\psi = \left\{ (z,\gamma) \in \mathbb{R}^N \times \mathbb{R} \,\middle|\, \psi(z) \leq \gamma \right\}. \quad (23)$$

Using this definition, conditions (19a) and (19b) represent the epigraph of the functions h_1 and h_2, respectively. More precisely, condition (19a) implies that for every $n \in \{1,\ldots,N\}$, $(\mathsf{S}_{n,1}, \mathsf{Z}_{n,1}) \in \operatorname{epi} h_1$. For a compact notation, we define $\mathbb{E}_1 = (\operatorname{epi} h_1)^N$ to be the product space such that

$$(\mathbf{S}_{:,1}, \mathbf{Z}_{:,1}) \in \mathbb{E}_1 \Leftrightarrow (\forall n \in \{1,\ldots,N\})\ (\mathsf{S}_{n,1}, \mathsf{Z}_{n,1}) \in \operatorname{epi} h_1. \quad (24)$$

Similarly, defining $\mathbb{E}_2 = (\operatorname{epi} h_2)^N$, condition (19b) is equivalent to

$$(\mathbf{S}_{:,2:4}, \mathbf{Z}_{:,2}) \in \mathbb{E}_2 \Leftrightarrow (\forall n \in \{1,\ldots,N\})\ (\mathbf{S}_{n,2:4}, \mathsf{Z}_{n,2}) \in \operatorname{epi} h_2. \quad (25)$$

Thus, the constraints (19a) and (19b) can be imposed as $\iota_{\mathbb{E}_1}(\mathbf{S}_{:,1}, \mathbf{Z}_{:,1})$ and $\iota_{\mathbb{E}_2}(\mathbf{S}_{:,2:4}, \mathbf{Z}_{:,2})$, respectively. Furthermore, to impose condition (19c), we introduce

$$\mathbb{V} = \left\{ \mathbf{Z} \in \mathbb{R}^{N\times 2} \,\middle|\, \left(\forall n \in \{1,\ldots,N\}\right) \mathsf{Z}_{n,1} + \mathsf{Z}_{n,2} \leq 0 \right\}. \quad (26)$$

Then, condition (19c) can be represented as an indicator function of the set $\mathbb{V}$. Finally, imposing the constraints (19a)–(19c) using their respective indicator functions leads to the following minimization problem

$$\underset{\substack{\mathbf{S}\in\mathbb{R}^{N\times 4},\\ \mathbf{Z}\in\mathbb{R}^{N\times 2}}}{\text{minimize}}\; f\left(\Phi(\mathbf{S})\right) + \iota_{\mathbb{U}}(\mathbf{S}) + \gamma\, g(\boldsymbol{\Psi}^\dagger \mathbf{S}) + \iota_{\mathbb{V}}(\mathbf{Z}) \\ + \iota_{\mathbb{E}_1}(\mathbf{S}_{:,1}, \mathbf{Z}_{:,1}) + \iota_{\mathbb{E}_2}(\mathbf{S}_{:,2:4}, \mathbf{Z}_{:,2}), \quad (27)$$

where $\gamma > 0$ is a free parameter only affecting the convergence speed.

It should be noted that the minimization problem (27) considers the SARA regularization and imposes the polarization constraint explicitly. We refer to this proposed method of joint Stokes imaging as Polarized SARA. Along the same lines, solving the problem

of Stokes imaging with SARA regularization but without polarization constraint (i.e. problem 18) is called Polarized SARA without constraint.

4.3 Algorithm formulation

In order to solve the resultant problem (27), we develop a method based on a primal–dual forward–backward algorithm, which offers a highly flexible and parallelizable structure (Condat 2013; Vũ 2013; Pesquet & Repetti 2015). The proposed algorithm is given in Algorithm 1. As described in Section 3.2, primal–dual methods consist in solving jointly the primal and dual problems. In our case, the primal problem to be solved is given in equation (27). This problem can be written in a compact form as

$$\underset{\substack{\mathbf{S}\in\mathbb{R}^{N\times 4},\\ \mathbf{Z}\in\mathbb{R}^{N\times 2}}}{\text{minimize}} \; q(\mathbf{S},\mathbf{Z}) + \gamma\, \widetilde{g}(\Psi^{\dagger}\mathbf{S},\mathbf{Z}) + \widetilde{f}\left(\Phi(\mathbf{S}),\mathbf{Z}\right) + l(\mathbf{S},\mathbf{Z}), \quad (28)$$

where,

$$\begin{aligned} q(\mathbf{S},\mathbf{Z}) &= \iota_{\mathbb{U}}(\mathbf{S}) + \iota_{\mathbb{V}}(\mathbf{Z}),\\ \widetilde{g}(\Psi^{\dagger}\mathbf{S},\mathbf{Z}) &= g(\Psi^{\dagger}\mathbf{S}),\\ \widetilde{f}\left(\Phi(\mathbf{S}),\mathbf{Z}\right) &= f\left(\Phi(\mathbf{S})\right),\\ l(\mathbf{S},\mathbf{Z}) &= \iota_{\mathbb{E}_1}(\mathbf{S}_{:,1},\mathbf{Z}_{:,1}) + \iota_{\mathbb{E}_2}(\mathbf{S}_{:,2:4},\mathbf{Z}_{:,2}). \end{aligned}$$

Then, according to Section 3.2 (for further detail, see, e.g. Komodakis & Pesquet 2015), the dual problem associated with (28) is given by

$$\begin{aligned} \underset{\substack{\mathbf{A}\in\mathbb{R}^{J\times 4},\mathbf{B}\in\mathbb{C}^{M\times 4},\\ \mathbf{C}\in\mathbb{R}^{N\times 4},\mathbf{D}\in\mathbb{R}^{N\times 2}}}{\text{minimize}} \; & q^*(-\Psi\mathbf{A} - \Phi^{\dagger}(\mathbf{B}) - \mathbf{C}, -\mathbf{D}) + \frac{1}{\gamma}\,\widetilde{g}^*(\mathbf{A},\mathbf{D}) \quad (29)\\ & + \widetilde{f}^*(\mathbf{B},\mathbf{D}) + l^*(\mathbf{C},\mathbf{D}). \end{aligned}$$

In problem (29), $\mathbf{A}\in\mathbb{R}^{J\times 4}$ is the dual variable corresponding to the non-smooth ℓ_1 term (the function g in problem (27)), $\mathbf{B}\in\mathbb{C}^{M\times 4}$ is the dual variable associated with the data fidelity term (the function f in problem 27), whereas $\mathbf{C}\in\mathbb{R}^{N\times 4}$ and $\mathbf{D}\in\mathbb{R}^{N\times 2}$ are associated with the indicator functions of the epigraphs of h_1 and h_2 in problem (27).

Using this primal–dual formulation, Algorithm 1 solves alternately for the above-mentioned primal and dual problems. In this regard, the algorithm can be seen as consisting of two major steps, denoted by: Primal updates and Dual updates. In each iteration $k\in\mathbb{N}$, it involves updating the primal variables $\mathbf{S}$ and $\mathbf{Z}$, followed by the update of the dual variables $\mathbf{A}$, $\mathbf{B}$, $\mathbf{C}$ and $\mathbf{D}$, as detailed in the following.

Algorithm 1 Primal-dual algorithm for joint Stokes imaging

1: **given** $\mathbf{S}^{(0)}\in\mathbb{R}^{N\times 4}$, $\mathbf{Z}^{(0)}\in\mathbb{R}^{N\times 2}$, $\mathbf{A}^{(0)}\in\mathbb{R}^{J\times 4}$, $\mathbf{B}^{(0)}\in\mathbb{R}^{M\times 4}$, $\mathbf{C}^{(0)}\in\mathbb{R}^{N\times 4}$, $\mathbf{D}^{(0)}\in\mathbb{R}^{N\times 2}$, $\gamma\mathbf{W}\in\mathbb{R}_{+}^{J\times 4}$

2: **repeat for** $k = 0, 1, \ldots$

Primal updates

3: $\mathbf{S}^{(k+1)} = \mathcal{P}_{\mathbb{U}}\left(\mathbf{S}^{(k)} - \tau\left(\Psi\mathbf{A}^{(k)} + \Phi^{\dagger}(\mathbf{B}^{(k)}) + \mathbf{C}^{(k)}\right)\right)$

4: $\mathbf{Z}^{(k+1)} = \mathcal{P}_{\mathbb{V}}\left(\mathbf{Z}^{(k)} - \tau\mathbf{D}^{(k)}\right)$

Dual updates

Promoting sparsity:

5: $\widetilde{\mathbf{A}}^{(k)} = \mathbf{A}^{(k)} + \rho_1\Psi^{\dagger}\left(2\,\mathbf{S}^{(k+1)} - \mathbf{S}^{(k)}\right)$

6: $\mathbf{A}^{(k+1)} = \widetilde{\mathbf{A}}^{(k)} - \rho_1\mathcal{T}_{\gamma\mathbf{W}/\rho_1}\left(\widetilde{\mathbf{A}}^{(k)}/\rho_1\right)$

Projecting onto ℓ_2 ball:

7: $\widetilde{\mathbf{B}}^{(k)} = \mathbf{B}^{(k)} + \rho_2\,\Phi\left(2\,\mathbf{S}^{(k+1)} - \mathbf{S}^{(k)}\right)$

8: $\mathbf{B}^{(k+1)} = \widetilde{\mathbf{B}}^{(k)} - \rho_2\mathcal{P}_{\mathbb{B}(\mathbf{Y},\epsilon)}\left(\widetilde{\mathbf{B}}^{(k)}/\rho_2\right)$

Performing epigraphical projection:

9: $\widetilde{\mathbf{C}}^{(k)} = \mathbf{C}^{(k)} + \rho_3\left(2\,\mathbf{S}^{(k+1)} - \mathbf{S}^{(k)}\right)$

10: $\widetilde{\mathbf{D}}^{(k)} = \mathbf{D}^{(k)} + \rho_3\left(2\,\mathbf{Z}^{(k+1)} - \mathbf{Z}^{(k)}\right)$

11: $\begin{bmatrix}\mathbf{C}_{:,1}^{(k+1)}\\ \mathbf{D}_{:,1}^{(k+1)}\end{bmatrix} = \begin{bmatrix}\widetilde{\mathbf{C}}_{:,1}^{(k)}\\ \widetilde{\mathbf{D}}_{:,1}^{(k)}\end{bmatrix} - \rho_3\,\mathcal{P}_{\mathbb{E}_1}\left(\frac{1}{\rho_3}\begin{bmatrix}\widetilde{\mathbf{C}}_{:,1}^{(k)}\\ \widetilde{\mathbf{D}}_{:,1}^{(k)}\end{bmatrix}\right)$

12: $\begin{bmatrix}\mathbf{C}_{:,2:4}^{(k+1)}\\ \mathbf{D}_{:,2}^{(k+1)}\end{bmatrix} = \begin{bmatrix}\widetilde{\mathbf{C}}_{:,2:4}^{(k)}\\ \widetilde{\mathbf{D}}_{:,2}^{(k)}\end{bmatrix} - \rho_3\,\mathcal{P}_{\mathbb{E}_2}\left(\frac{1}{\rho_3}\begin{bmatrix}\widetilde{\mathbf{C}}_{:,2:4}^{(k)}\\ \widetilde{\mathbf{D}}_{:,2}^{(k)}\end{bmatrix}\right)$

13: **until convergence**

4.3.1 *Primal updates*

In Algorithm 1, the primal variables are incremented using steps 3 and 4. These updates have a structure reminiscent of the forward–backward steps. More precisely, the forward–backward step consists of alternating between a gradient step and a proximity (or projection) step, whereas in the absence of any smooth term, only the proximity step is performed. This structure can be observed in the update of $\mathbf{S}$ (i.e. step 3), where a projection on to the set $\mathbb{U}$ is carried out. We can notice that an additive term appears in this update. This additional term allows us to take into account the dual variables $\mathbf{A}$, $\mathbf{B}$ and $\mathbf{C}$, associated with the sparsity prior, the data fidelity term and the epigraphical constraints, respectively. The same analogy can be observed for updating step 4 of the variable $\mathbf{Z}$. This update takes into account the dual variable $\mathbf{D}$ associated with the epigraphical constraints, followed by a projection on to the set $\mathbb{V}$.

In particular for steps 3 and 4, the projections on to the sets $\mathbb{U}$ and $\mathbb{V}$, respectively, need to be performed. First, for any matrix $\mathbf{X}$ of size $N\times 4$, the projection on to the set $\mathbb{U}$ is simply given by

$$\mathcal{P}_{\mathbb{U}}(\mathbf{X}) = \mathrm{Re}\,(\mathbf{X}), \quad (30)$$

where the operator Re(.) provides the real part of its argument.

Secondly, using Proposition 2.1 from Chierchia et al. (2015), the projection on to the set $\mathbb{V}$ is performed as

$$(\forall\,\mathbf{U}\in\mathbb{R}^{N\times 2}) \quad \mathcal{P}_{\mathbb{V}}(\mathbf{U}) = \widetilde{\mathbf{U}}, \quad (31)$$

where $\widetilde{\mathbf{U}}\in\mathbb{R}^{N\times 2}$ is defined such that, for every $n\in\{1,\ldots,N\}$,

$$\begin{aligned} &\left(\widetilde{\mathrm{U}}_{n,1},\widetilde{\mathrm{U}}_{n,2}\right)\\ &\quad = \begin{cases} (\mathrm{U}_{n,1},\mathrm{U}_{n,2}), & \text{if } \mathrm{U}_{n,1}+\mathrm{U}_{n,2}\le 0,\\ \frac{1}{2}(\mathrm{U}_{n,1}-\mathrm{U}_{n,2},\mathrm{U}_{n,2}-\mathrm{U}_{n,1}), & \text{otherwise.}\end{cases} \end{aligned} \quad (32)$$

4.3.2 *Dual updates*

The dual variables are updated in steps 5–12 of Algorithm 1. At each iteration k, it requires the evaluation of the proximity operators of the associated functions.

Sparsity prior. Steps 5 and 6 consist of updating the dual variable $\mathbf{A}$ associated with the sparsity prior defined in equation (14). In particular, step 6 needs to perform the proximity operator of the ℓ_1 norm, which corresponds to the soft-thresholding operation (Chaux et al. 2007), using the soft-threshold sizes given by $\gamma\mathbf{W} \in \mathbb{R}_+^{J\times 4}$. Furthermore, $\mathcal{T}$ stands for the soft-thresholding operator and is defined as

$$(\forall\, \mathbf{A} \in \mathbb{R}^{J\times 4}) \quad \mathcal{T}_{\gamma\mathbf{W}/\rho_1}\left(\mathbf{A}/\rho_1\right) = \mathbf{H}, \tag{33}$$

where $\mathbf{H} \in \mathbb{R}^{J\times 4}$ is defined as follows

$$(\forall i \in \{1,2,3,4\}) \quad \mathbf{H}_{:,i} = \mathrm{prox}_{\rho_1^{-1}\gamma\mathbf{W}_{:,i}\|.\|_1}\left(\mathbf{A}_{:,i}\right). \tag{34}$$

The soft-thresholding operation is performed component-wise. Therefore, in equation (34), with $j \in \{1,\ldots,J\}$, the jth component of each vector $\mathbf{H}_{:,i}$ is given by

$$\mathsf{H}_{j,i} = \begin{cases} -\mathsf{A}_{j,i} + \gamma\mathsf{W}_{j,i}/\rho_1\,, & \text{if } \mathsf{A}_{j,i} < -\gamma\mathsf{W}_{j,i}/\rho_1\,, \\ 0, & \text{if } -\gamma\mathsf{W}_{j,i}/\rho_1 \le \mathsf{A}_{j,i} \\ & \quad \le \gamma\mathsf{W}_{j,i}/\rho_1\,, \\ \mathsf{A}_{j,i} - \gamma\mathsf{W}_{j,i}/\rho_1\,, & \text{otherwise.} \end{cases} \tag{35}$$

This operation consists of forcing the elements, which are smaller than some threshold, to zero, while reducing the rest of the elements by this threshold value. Therefore, iteration-by-iteration, it removes the smaller values and finally, only the elements having significant values are left, hence promoting sparsity

Data fidelity. Steps 7 and 8 are involved in the update of the dual variable $\mathbf{B}$ corresponding to the data fidelity term given in equation (13). This update involves the projection on to the ℓ_2 ball $\mathbb{B}(\mathbf{Y},\epsilon)$ of radius ϵ and centred in $\mathbf{Y}$. For any matrix $\mathbf{B} \in \mathbb{C}^{M\times 4}$, the corresponding projection is given by

$$\mathcal{P}_{\mathbb{B}(\mathbf{Y},\epsilon)}(\mathbf{B}/\rho_2) = \begin{cases} \epsilon\dfrac{(\mathbf{B}/\rho_2)-\mathbf{Y}}{\|(\mathbf{B}/\rho_2)-\mathbf{Y}\|_2} + \mathbf{Y}, & \text{if } \|(\mathbf{B}/\rho_2)-\mathbf{Y}\|_2 > \epsilon, \\ \mathbf{B}/\rho_2, & \text{otherwise.} \end{cases} \tag{36}$$

Epigraphical projections and polarization constraint. Steps 9–12 consist of updating the dual variables $\mathbf{C}$ and $\mathbf{D}$, which are associated with the epigraphical projections on the functions h_1 and h_2. As previously mentioned, these projections are required to enforce the polarization constraint. In particular, in step 11, the vectors $(\widetilde{\mathbf{C}}_{:,1}, \widetilde{\mathbf{D}}_{:,1})$ are needed to be projected on to the epigraph of h_1, while in step 12, the projection of $(\widetilde{\mathbf{C}}_{:,2:4}, \widetilde{\mathbf{D}}_{:,2})$ on to the epigraph of h_2 is required. These projections can be performed in the following manner. First, for any two variables $(\boldsymbol{c},\boldsymbol{d}) \in (\mathbb{R}^N)^2$, following Chierchia et al. (2015), the projection on to the epigraph of the function h_1 reduces to

$$\mathcal{P}_{\mathbb{E}_1}(\boldsymbol{c},\boldsymbol{d}) = (\widetilde{c}_n, \widetilde{d}_n)_{1\le n\le N}, \tag{37}$$

where

$$(\widetilde{c}_n, \widetilde{d}_n) = \begin{cases} (c_n, d_n), & \text{if } c_n + d_n \ge 0, \\ \left(\frac{1}{2}(c_n - d_n), \frac{d_n - c_n}{2}\right), & \text{otherwise.} \end{cases} \tag{38}$$

Secondly, for every $(\mathbf{R} \in \mathbb{R}^{N\times 3}, \boldsymbol{d} \in \mathbb{R}^N)$, the projection on to the epigraph of the function h_2 is given by

$$\mathcal{P}_{\mathbb{E}_2}(\mathbf{R},\boldsymbol{d}) = (\widetilde{\mathbf{R}}_{n,:}, \widetilde{d}_n)_{1\le n\le N}, \tag{39}$$

such that

$$(\widetilde{\mathbf{R}}_{n,:}, \widetilde{d}_n) = \begin{cases} (\mathbf{0}, 0), & \text{if } \|\mathbf{R}_{n,:}\|_2 < -d_n, \\ (\mathbf{R}_{n,:}, d_n), & \text{if } \|\mathbf{R}_{n,:}\|_2 < d_n, \\ \alpha_n\left(\mathbf{R}_{n,:}, \|\mathbf{R}_{n,:}\|_2\right), & \text{otherwise,} \end{cases} \tag{40}$$

where $\alpha_n = \frac{1}{2}\left(1 + \frac{d_n}{\|\mathbf{R}_{n,:}\|_2}\right)$ (Chierchia et al. 2015).

4.3.3 *Convergence properties*

The choice of the step sizes τ, ρ_1, ρ_2 and ρ_3 governs the convergence of Algorithm 1 to the solution of the minimization problem (27). More precisely, these parameters should be chosen in a manner that the following holds (Pesquet & Repetti 2015)

$$\frac{1}{\tau} - \rho_1\,\|\Psi\|_{\mathrm{sp}}^2 - \rho_2\|\Phi\|_{\mathrm{sp}}^2 - \rho_3 \ge 0, \tag{41}$$

where $\|.\|_{\mathrm{sp}}$ denotes the spectral norm of its argument. Then, under this condition, the sequence of iterates $(\mathbf{S}^{(k)})_{k\in\mathbb{N}}$ generated by Algorithm 1 converges to a solution to problem (27).

Additional remarks can be made regarding the proposed approach. The whole procedure of updating primal variables followed by the dual variables in Algorithm 1 is repeated until the required convergence criterion, defined by the user, is met. Furthermore, it is worth mentioning that the different steps involved in Algorithm 1 can be implemented in parallel for each vector within the defined matrices. Therefore, it presents a highly parallelizable algorithm.

4.3.4 *Reweighting scheme*

As discussed earlier, we aim to solve the weighted ℓ_1 minimization problem iteratively, and hence approaching the solution in the ℓ_0 sense. More precisely, each reweighting iteration, indexed by $l \in \mathbb{N}$, consists of solving the weighted ℓ_1 minimization problem (27) using Algorithm 1. The weights for each iteration are computed from the previous solution of the Stokes images as

$$(\forall j \in \{1,\ldots,J\}) \quad \mathsf{W}_{j,i}^{(l+1)} = \frac{\delta^{(l+1)}}{\delta^{(l+1)} + |[\Psi^\dagger\mathbf{S}^{(l)}]_{j,i}|}\,, \tag{42}$$

where $i \in \{1,\ldots,4\}$ and $\delta^{(l+1)} > 0$ is decreased iteration-by-iteration such that $\delta^{(l+1)} \to 0$ when $l \to +\infty$, and hence the weighted ℓ_1 norm approaches to the ℓ_0 norm. The newly computed weights are used to update the soft-threshold sizes as $\gamma\mathbf{W}^{(l+1)}$.

To initialize the weights, recall that one of the benefits of using this reweighting scheme is to avoid the tuning of any additional regularization parameters. Keeping this in mind, Algorithm 1 is used to solve the problem consisting of only the data fidelity term and the positivity constraint, without imposing the sparsity and polarization constraint, i.e. problem (18) with function $g = 0$. This corresponds to solving a constrained version of the non-negative least-squares problem. Formally, in the algorithm, it consists of updating the primal variable $\mathbf{S}$ and the dual variable $\mathbf{B}$, with the rest of the primal and dual variables appearing in Algorithm 1 taken to be zero, and the set $\mathbb{U}$ modified to set $\mathbb{U}'$ to take into account positivity of the total intensity image. The solutions obtained are then used to compute the weights (as defined in equation (42)) for $l = 1$ and hence the soft-thresholding sizes for the first reweighting iteration. Subsequent reweighting iterations solve for the problem

(27) by passing on the updated sizes along with the solutions of the primal and dual variables from the previous iteration to Algorithm 1. The resultant reweighting scheme is described in Algorithm 2. This process is repeated until convergence.

Algorithm 2 Reweighting scheme

1: **given** $\mathbf{S}^{(0)}, \mathbf{Z}^{(0)}, \mathbf{A}^{(0)}, \mathbf{B}^{(0)}, \mathbf{C}^{(0)}, \mathbf{D}^{(0)}, \gamma\mathbf{W}^{(0)}$
2: **repeat for** $l = 0, 1, \ldots$
3: $[\mathbf{S}^{(l+1)}, \mathbf{Z}^{(l+1)}, \mathbf{A}^{(l+1)}, \mathbf{B}^{(l+1)}, \mathbf{C}^{(l+1)}, \mathbf{D}^{(l+1)}]$ = Algorithm 1
4: $\forall i \in \{1, 2, 3, 4\}$, **compute** $\mathbf{W}_{:,i}^{(l+1)}$ as per equation (42)
5: **until convergence**

4.4 Polarization constraint for TV-based problems

In the context of EHT imaging for full polarization, Akiyama et al. (2017a) consider independent problems for each of the Stokes parameters. This is achieved by post-multiplying equation (3) with $\mathbf{L}^{-1}$, the inverse of the operator $\mathbf{L}$, thereby converting the brightness matrix back to the Stokes matrix and giving $\mathbf{Y}\mathbf{L}^{-1} = \widetilde{\Phi}(\overline{\mathbf{S}}) + \mathbf{E}\mathbf{L}^{-1}$. Here $\widetilde{\Phi}$ is a modified operator incorporating $\mathbf{L}^{-1}$ in the operator Φ. In this manner, in the absence of DDEs, each column of $\widetilde{\mathbf{Y}} = \mathbf{Y}\mathbf{L}^{-1}$ corresponds to the measured visibilities related to the respective Stokes parameter in the matrix $\overline{\mathbf{S}}$. Akiyama et al. (2017a) then propose to solve the following minimization problem

$$\underset{\mathbf{S}\in\mathbb{R}^{N\times 4}}{\text{minimize}} \ \frac{1}{2}\|\widetilde{\mathbf{Y}} - \widetilde{\Phi}(\mathbf{S})\|_2^2 + \iota_{\mathbb{U}'}(\mathbf{S}) + \check{g}(\Psi^\dagger\mathbf{S}), \tag{43}$$

where the unconstrained problem formulation is used and the data fidelity term is given by the squared ℓ_2 term (the first term in (43)). The polarization constraint is not imposed, justifying the use of the set $\mathbb{U}'$ to impose positivity of the total intensity image. Furthermore, the third term, $\check{g}(\Psi^\dagger\mathbf{S})$ in problem (43) is the sparsity prior imposing the sparsity of the sought images in some sparsifying dictionary. In this regard, Akiyama et al. (2017a) show that the TV and ℓ_1 +TV sparsifying regularizations are effective in producing super-resolved images and lead to better reconstruction quality than using the standard CLEAN method. For these regularizations, they have considered the isotropic TV norm. Basically, the TV norm is defined for a two-dimensional (2D) image $\mathbf{U} \in \mathbb{R}^{N_1\times N_2}$ as the $\ell_{2,1}$ norm of the horizontal and vertical gradients of this image (Rudin et al. 1992).[2] More formally, it is given by

$$\begin{aligned}\|\mathbf{U}\|_{\text{TV}} &= \|\nabla\mathbf{U}\|_{2,1} \\ &= \sum_{n_1=1}^{N_1}\sum_{n_2=1}^{N_2}\sqrt{|[\nabla_x\mathbf{U}]_{n_1,n_2}|^2 + |[\nabla_y\mathbf{U}]_{n_1,n_2}|^2},\end{aligned} \tag{44}$$

where $\nabla = [\nabla_x, \nabla_y]$ is the concatenation of the horizontal gradient operator $\nabla_x : \mathbb{R}^{N_1\times N_2} \to \mathbb{R}^{N_1\times N_2}$ and the vertical gradient operator $\nabla_y : \mathbb{R}^{N_1\times N_2} \to \mathbb{R}^{N_1\times N_2}$.

[2]In the current work, the images are represented in vectorized form of dimension $N = N_1 \times N_2$. However, the 2D images can easily be obtained by reshaping these vectors.

We hereby propose to generalize the minimization problem (43) solved by Akiyama et al. (2017a) to incorporate explicitly the polarization constraint. It amounts to

Algorithm 3 Primal-dual algorithm to solve problem (45)

1: **given** $\mathbf{S}^{(0)} \in \mathbb{R}^{N\times 4}$, $\mathbf{Z}^{(0)} \in \mathbb{R}^{N\times 2}$, $\mathbf{A}^{(0)} \in \mathbb{R}^{J\times 4}$, $\mathbf{C}^{(0)} \in \mathbb{R}^{N\times 4}$, $\mathbf{D}^{(0)} \in \mathbb{R}^{N\times 2}$
2: **repeat for** $k = 0, 1, \ldots$

Primal updates

3: $\mathbf{S}^{(k+1)} = \mathcal{P}_{\mathbb{U}}\left(\mathbf{S}^{(k)} - \tau\widetilde{\Phi}^\dagger(\widetilde{\Phi}(\mathbf{S}^{(k)}) - \widetilde{\mathbf{Y}}) - \tau(\Psi\mathbf{A}^{(k)} + \mathbf{C}^{(k)})\right)$
4: $\mathbf{Z}^{(k+1)} = \mathcal{P}_{\mathbb{V}}\left(\mathbf{Z}^{(k)} - \tau\mathbf{D}^{(k)}\right)$

Dual updates

Promoting sparsity:

5: $\widetilde{\mathbf{A}}^{(k)} = \mathbf{A}^{(k)} + \rho_1\Psi^\dagger\left(2\,\mathbf{S}^{(k+1)} - \mathbf{S}^{(k)}\right)$
6: $\mathbf{A}^{(k+1)} = \widetilde{\mathbf{A}}^{(k)} - \rho_1\mathcal{T}_{\boldsymbol{\Lambda}/\rho_1}\left(\widetilde{\mathbf{A}}^{(k)}/\rho_1\right)$

Performing epigraphical projection:

7: $\widetilde{\mathbf{C}}^{(k)} = \mathbf{C}^{(k)} + \rho_3\left(2\,\mathbf{S}^{(k+1)} - \mathbf{S}^{(k)}\right)$
8: $\widetilde{\mathbf{D}}^{(k)} = \mathbf{D}^{(k)} + \rho_3\left(2\,\mathbf{Z}^{(k+1)} - \mathbf{Z}^{(k)}\right)$
9: $\begin{bmatrix}\mathbf{C}_{:,1}^{(k+1)} \\ \mathbf{D}_{:,1}^{(k+1)}\end{bmatrix} = \begin{bmatrix}\widetilde{\mathbf{C}}_{:,1}^{(k)} \\ \widetilde{\mathbf{D}}_{:,1}^{(k)}\end{bmatrix} - \rho_3\,\mathcal{P}_{\mathbb{E}_1}\left(\frac{1}{\rho_3}\begin{bmatrix}\widetilde{\mathbf{C}}_{:,1}^{(k)} \\ \widetilde{\mathbf{D}}_{:,1}^{(k)}\end{bmatrix}\right)$
10: $\begin{bmatrix}\mathbf{C}_{:,2:4}^{(k+1)} \\ \mathbf{D}_{:,2}^{(k+1)}\end{bmatrix} = \begin{bmatrix}\widetilde{\mathbf{C}}_{:,2:4}^{(k)} \\ \widetilde{\mathbf{D}}_{:,2}^{(k)}\end{bmatrix} - \rho_3\,\mathcal{P}_{\mathbb{E}_2}\left(\frac{1}{\rho_3}\begin{bmatrix}\widetilde{\mathbf{C}}_{:,2:4}^{(k)} \\ \widetilde{\mathbf{D}}_{:,2}^{(k)}\end{bmatrix}\right)$
11: **until convergence**

$$\begin{aligned}\underset{\substack{\mathbf{S}\in\mathbb{R}^{N\times 4},\\ \mathbf{Z}\in\mathbb{R}^{N\times 2}}}{\text{minimize}} \ &\frac{1}{2}\|\widetilde{\mathbf{Y}} - \widetilde{\Phi}(\mathbf{S})\|_2^2 + \iota_{\mathbb{U}}(\mathbf{S}) + \check{g}(\Psi^\dagger\mathbf{S}) + \iota_{\mathbb{V}}(\mathbf{Z}) \\ &+\iota_{\mathbb{E}_1}(\mathbf{S}_{:,1}, \mathbf{Z}_{:,1}) + \iota_{\mathbb{E}_2}(\mathbf{S}_{:,2:4}, \mathbf{Z}_{:,2}).\end{aligned} \tag{45}$$

This problem can be solved by using a modified version of the primal–dual method proposed in Algorithm 1. In particular, Algorithm 1 can incorporate any convex sparsity regularization function, and can be adapted for the unconstrained problem of interest. The resultant algorithm is provided in Algorithm 3, consisting of the following amendments made in Algorithm 1.

(i) While Algorithm 1 has been provided for the constrained formulation with the data fidelity term defined in equation (13), problem (45) where the data consistency is instead ensured by a differentiable squared ℓ_2 term, can still be solved. More precisely, the update of variable $\mathbf{B}$ in Algorithm 1 is no longer required, instead the gradient term $(\widetilde{\Phi}^\dagger(\widetilde{\Phi}(\mathbf{S}) - \widetilde{\mathbf{Y}}))$ is added in the update of the variable $\mathbf{S}$, as shown in step 3 of Algorithm 3.

(ii) Regarding the sparsity prior, depending on the chosen regularization, the corresponding thresholding operator $\mathcal{T}$ and the dictionary $\mathbf{\Psi}$ needs to be modified in step 6. With this in mind, either of the TV and ℓ_1 +TV sparsifying regularizations can be taken into account in Algorithm 3 as follows.

TV regularization. The sparsity prior is given by $\check{g}(\mathbf{\Psi}^\dagger \mathbf{S}) = \sum_{i=1}^{4} \mu_i \|\nabla \mathbf{S}'_i\|_{2,1}$, where $\mathbf{S}'_i$ is the reshaped matrix form of the vector $\mathbf{S}_{:,i}$ and for every $i \in \{1, 2, 3, 4\}$, $\mu_i > 0$ is the regularization parameter. Thus, in Algorithm 3, $\mathbf{\Psi} = \nabla$ and the operator $\mathcal{T} = \mathcal{T}_{\rm TV}$ is the proximity operator for the TV norm (Chambolle & Lions 1997; Beck & Teboulle 2009b), using the threshold-size $\mathbf{\Lambda} = [\mu_1, \mu_2, \mu_3, \mu_4]$ in step 6.

ℓ_1 +TV regularization. It consists of two terms, $\check{g}(\mathbf{\Psi}^\dagger \mathbf{S}) = \sum_{i=1}^{4} \upsilon_{1,i} \|\mathbf{S}_{:,i}\|_1 + \sum_{i=1}^{4} \upsilon_{2,i} \|\nabla \mathbf{S}'_i\|_{2,1}$, with $\upsilon_{1,i}$ and $\upsilon_{2,i} > 0$. The first term (i.e. the ℓ_1 norm) imposes sparsity of the underlying images in the Dirac basis. The second term (i.e. the TV term) promotes the sparsity in the gradient domain (44). As a result, in this case, the sparsifying dictionary $\mathbf{\Psi} = [\mathbf{1}, \nabla]$ is the concatenation of the identity matrix (Dirac basis) and the gradient basis, respectively. Similarly, the operator $\mathcal{T} = [\mathcal{T}_{\mathbf{1}}, \mathcal{T}_{\rm TV}]$ is the concatenation of the proximity operators corresponding to the ℓ_1 and the TV norms, associated with the thresholding sizes $\boldsymbol{\upsilon}_1 = [\upsilon_{1,1}, \upsilon_{1,2}, \upsilon_{1,3}, \upsilon_{1,4}]$ and $\boldsymbol{\upsilon}_2 = [\upsilon_{2,1}, \upsilon_{2,2}, \upsilon_{2,3}, \upsilon_{2,4}]$, respectively (i.e. $\mathbf{\Lambda} = [\boldsymbol{\upsilon}_1, \boldsymbol{\upsilon}_2]$ in step 6).

We can notice that the same algorithm can be used to solve problem (43) as well wherein the polarization constraint is not imposed and only steps 3, 5 and 6 in Algorithm 3 need to be executed.

Lastly, regarding the terminology, solving problem (45) considering TV regularization (resp. ℓ_1 + TV) is referred to as the TV (resp. ℓ_1 + TV) problem with constraint. Similarly, solving problem (43) with TV regularization (resp. ℓ_1 + TV) is called the TV (resp. ℓ_1 + TV) problem without constraint.

5 SIMULATIONS AND RESULTS

In this section, we discuss the considered simulation settings and we describe the different cases for simulations. We then investigate the performance of the proposed Polarized SARA method, implemented in MATLAB[3], on simulated EHT data sets.

5.1 Simulation set-up

Without any loss of generality for the proposed algorithm, we consider the idealistic case and work in the absence of DDEs. In such a scenario, the Mueller matrix is essentially the identity matrix, and the measurement operator takes the form

$$\Phi(\overline{\mathbf{S}}) = \mathbf{\Theta} \cdot \mathbf{GFZ}\overline{\mathbf{S}}\,\mathbf{L} \tag{46}$$

where $\cdot$ denotes the Hadamard product. More specifically, the operator $\mathbf{L} \in \mathbb{C}^{4\times4}$ acts on the Stokes matrix $\overline{\mathbf{S}}$ to give the brightness matrix, as described in Section 2. Once the brightness matrix is obtained, the zero padding operator $\mathbf{Z} \in \mathbb{C}^{\alpha N \times N}$ is used to oversample the image contained in each column of the brightness matrix, by a factor of α in each dimension. Then, the task is to compute the Fourier transform of the oversampled images at the spatial frequencies sampled by the interferometer. However, evaluating the Fourier transform directly at these sampled points incurs a high computational cost. Thus, we use a fast implementation of the Fourier transform in terms of a fast Fourier transform (FFT), performed by a matrix $\mathbf{F} \in \mathbb{C}^{\alpha N \times \alpha N}$. Because FFT provides discrete Fourier coefficients, the operation of degridding these discrete Fourier points to the continuous samples is performed by a matrix $\mathbf{G} \in \mathbb{C}^{M \times \alpha N}$. More precisely, each row of this matrix $\mathbf{G}$ consists of convolution kernels, which are modelled with compact support in the Fourier domain (Fessler & Sutton 2003). Moreover, the matrix $\mathbf{Z}$ consists of oversampling and scaling of the sought images in order to compensate for the interpolation errors introduced by the matrix $\mathbf{G}$. Finally, the noise statistics are incorporated via the matrix $\mathbf{\Theta} \in \mathbb{R}^{M\times4}$. Its elements are the inverse of the square root of the noise variances corresponding to the respective measurements in the matrix $\mathbf{Y}$. In this case, the measurement matrix $\mathbf{Y}$ is also considered as the result of the Hadamard product between $\mathbf{\Theta}$ and the unweighted measurements from the radio interferometer.

It can be noticed that using equation (46), in the absence of DDEs, the measurement model given in equation (3) can be seen as the Fourier transform of the brightness matrix $\overline{\mathbf{S}}\mathbf{L}$ computed at the sampled frequencies. It is to be emphasized that in this paper we work with complex visibilities. As such, the proposed approach can be applied to complex visibility measurements obtained by any radio interferometer. We also note that in the context of VLBI, including the future observations made by EHT, the visibility phase cannot be measured. In this scenario, our technique can still be applied on the self-calibrated data. Another possibility is to work with phase-insensitive observables, as in the case of optical interferometry (OI) (Thiébaut & Giovannelli 2010). Furthermore, for these measurements, the noise bound ϵ is difficult to be estimated, and either the adaptive scheme developed in Dabbech et al. (2017a) can be applied or the unconstrained formulation (7) of the underlying minimization problem can be considered. In this respect, the proposed method can be combined with other sparse modelling techniques in OI (Akiyama et al. 2017b; Birdi, Repetti & Wiaux 2017), which is beyond the scope of the current paper.

With these measurement settings, we perform tests on the EHT $u-v$ coverage, as shown in Fig. 1. This realistic coverage, adopted from Akiyama et al. (2017a,b), corresponds to the measurements made at wavelength $\lambda = 1.3$ mm (i.e. observation frequency of 230 GHz), using a VLBI array consisting of six stations. In this case, the maximum observation baseline, $\mathrm{B}_{\max} = 7.2\ \mathrm{G}\lambda$. Furthermore, we consider two sets of images based on physically motivated models of M87 radio emissions at a wavelength of 1.3 mm. The first set of images consists of a forward-jet model, which was initially developed by Broderick & Loeb (2009). We use the version of this model presented in Lu et al. (2014), coherent with the EHT observations at the considered wavelength. The second set of images involves a counter-jet model. It is based on general relativistic magnetohydrodynamic (GRMHD) simulation results (Dexter, McKinney & Agol 2012) and polarimetric radiative transfer calculations (Dexter 2016). We focus on imaging of Stokes I, Q and U parameters, as done in Akiyama et al. (2017a), by considering only three columns in the sought Stokes matrix. The two sets of images are displayed in Fig. 2 in the first and second columns, respectively. In both cases, the true Stokes I, Q and U images are presented along with the linear polarization image P, respectively, in rows one to four. For both these sets, we consider the image size $N = 100 \times 100$ with the field of view of 200 μas. Then, the resultant pixel size of 2 μas corresponds to a scale of $\sim 0.21 R_s$. For both sets of model images, we simulate the noisy measurements as per equation (3)

[3]The MATLAB code is available at https://basp-group.github.io/stokes-imaging/.

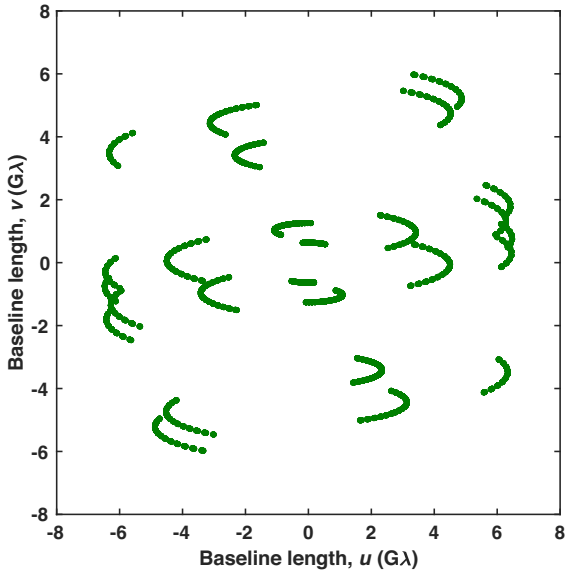

Figure 1. The EHT $u - v$ coverage used for simulations, taken from Akiyama et al. (2017a,b). It corresponds to the meaurements made at 1.3 mm (230 GHz) using six stations of the VLBI array.

with the measurement operator given by equation (46). We consider the measurements related to each column of the brightness matrix to be corrupted by a Gaussian noise with the same variance σ^2, where $\sigma = 5 \times 10^{-3}$ Jy. The scale of the chosen variance is broadly consistent with the EHT settings considered in Akiyama et al. (2017a). Additionally, though we consider the same variance for all the visibilities, the same approach also works with different variances, by using suitable values in the matrix $\boldsymbol{\Theta}$. In the considered settings, the residual norm resembles the χ^2 distribution with $8M$ degrees of freedom, and the bound ϵ for the ℓ_2 ball $\mathbb{B}$ defined in equation (13) can be determined from the noise variance $\sigma^2/2$ of the real and imaginary parts of the noise. We thus set this bound as $\epsilon^2 = (8M + 2\sqrt{2(8M)})\sigma^2/2$, where the bound ϵ^2 is taken to be two standard deviations above the mean of the χ^2 distribution (Carrillo et al. 2012).

5.2 Computational complexity

In each iteration $k \in \mathbb{N}$ of Algorithm 1, the major computational burdens come from the application of the measurement operator Φ and of the discrete wavelet transforms (DWT) $\boldsymbol{\Psi}$, while enforcing data fidelity and sparsity, respectively. In particular, the usage of the measurement operator in step 7 (and its adjoint in step 3) can be broadly split into the following: (i) computing the FFT of oversampled images contained in columns of the underlying matrix, each such image requiring a complexity of $\mathcal{O}(\alpha N \log \alpha N)$; (ii) applying the linear operator $\mathbf{G}$ with complexity of $\mathcal{O}(n_s M \alpha N)$ for each Fourier transformed image. Here, n_s is the sparsity percentage of each row of $\mathbf{G}$, due to the compact support convolution kernels used to reduce its computational burden. For large data sets having $M \gg N$, the term (ii) dominates in the computational cost. Concerning the sparsity operation, the major computational load comes by the application of the DWT in step 3 (and its adjoint in step 5), where we use its fast implementation providing a complexity of $\mathcal{O}(N)$ considering compactly supported wavelets (Daubechies & Sweldens 1998; Mallat 2009). Thus, for a dictionary $\boldsymbol{\Psi}$ consisting of n_b basis, it requires $\mathcal{O}(N)$ computations for each basis and each image stored in the underlying matrix. In the current code, we apply the sparsifying dictionary $\boldsymbol{\Psi}$ (and its adjoint) in parallel for each such image. Regarding the remaining steps in Algorithm 1, which involve performing projections on to the respective sets, each such projection scales linearly with the size of the argument matrix.

Investigation of the MATLAB code indicated that the epigraphical projections to impose the polarization constraint do not add much to the computational cost and thus Polarized SARA takes about the same time to converge as Polarized SARA without constraint. More specifically, in the current simulation settings, the MATLAB code takes a few hours in total, consisting of 10 reweighting iterations, to provide the final estimates of the Stokes parameters. We also note that larger data sets will incur a high computational cost and thus more time to converge to the solutions. It is worth mentioning that, mimicking the distributed primal–dual algorithm developed by Onose et al. (2016) for Stokes I reconstruction, most of the steps in Algorithm 1 can be distributed and parallelized. Working in this direction, a scalable version of the Polarized SARA approach has been presented in Birdi, Repetti & Wiaux (2018).

5.3 Effect of polarization constraint

As previously discussed in Section 4.1, the polarization constraint needs to be satisfied by the Stokes images to avoid unphysical reconstructions. To validate the importance of imposing this constraint explicitly in the reconstruction process, we perform tests with and without this constraint. The case of imposing this constraint (i.e. Polarized SARA) consists of solving the minimization problem (27) using Algorithm 2 with each reweighting iteration consisting of implementing Algorithm 1. On the contrary, Polarized SARA without constraint implies solving the minimization problem (18). In this context, Algorithm 1 can still be used to solve the weighted ℓ_1 minimization problems within the reweighting scheme. However, Algorithm 1 is employed to solve only for the Stokes matrix $\mathbf{S}$ (step 3), taking into account only the sparsity prior (steps 5 and 6) and the data fidelity term (steps 7 and 8). Additionally, recall that in the absence of the polarization constraint, the positivity of the Stokes I image is taken into account by the use of the modified set $\mathbb{U}'$ (17). In step 3 of Algorithm 1, the projection needs to be performed on this set. This projection also consists of taking the real part of its arguments as described in equation (30), with an extra step of considering only the positive values for Stokes I, i.e. $\mathbf{X}_{:,1} = \max\{\mathrm{Re}(\mathbf{X}_{:,1}), \mathbf{0}\}$.

In order to compare the tests performed with and without imposing the polarization constraint, we keep track of the pixels not satisfying this constraint (4). In particular, it consists of analysing the polarization error image, $\boldsymbol{p} \in \mathbb{R}^N_+$, where, for every $n \in \{1, \ldots, N\}$,

$$p_n = \begin{cases} -\mathbf{S}_{n,1} + \|\mathbf{S}_{n,2:3}\|_2, & \text{if } -\mathbf{S}_{n,1} + \|\mathbf{S}_{n,2:3}\|_2 > \zeta, \\ 0, & \text{otherwise.} \end{cases}$$

Basically, this image is generated by taking the difference between the linear polarization intensity image and the total intensity image, where only the pixels with values larger than some threshold ζ are retained, while the others are put to zero. In essence, this image is a representation of the pixels not satisfying the polarization constraint (4), and having values greater than ζ. The value of ζ is taken to be three times the rms noise, which is estimated from the residual image. Thus, by considering this threshold, the pixels with values

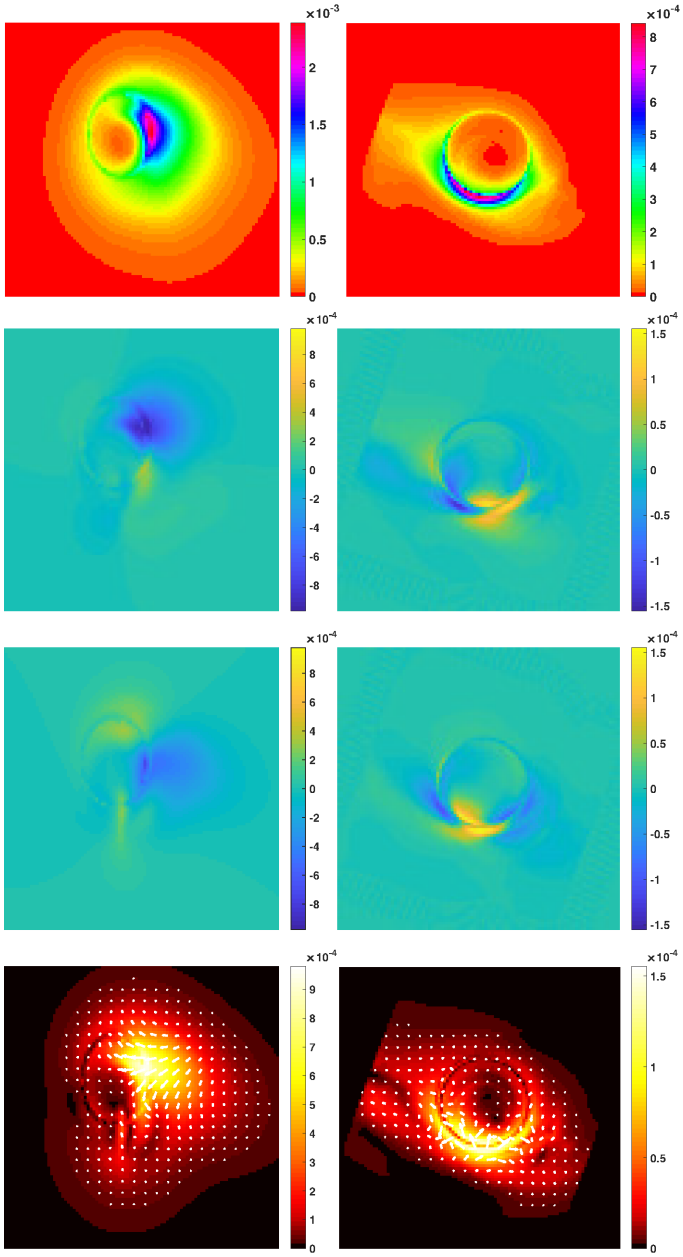

Figure 2. The two sets of ground-truth images used for performing simulations. The first column corresponds to the forward-jet model images (Broderick & Loeb 2009; Lu et al. 2014). The second column corresponds to the counter-jet model images (Dexter et al. 2012). For both columns, each row shows the following images: Stokes I (first row), Stokes Q (second row), Stokes U (third row) and the linear polarization image P (fourth row). For the latter, the electric vector polarization angle (EVPA) distribution is shown by white bars, plotted over the linear polarization intensity ($|P|$). All the images are shown in linear scale.

smaller than the noise level are discarded. Finally, we denote the percentage of the non-zero pixels in the image $\boldsymbol{p}$ by N_p, where $N_p \in [0, 100]$.

5.4 Comparison with the other methods

In the context of EHT imaging for full polarization, as mentioned earlier, the work by Akiyama et al. (2017a) represents the only existing method within the sparse modelling framework, aiming to solve the problem (43). In Section 4.4, we have proposed to generalize this problem by taking into account the polarization constraint and hence solving for problem (45). Keeping these in mind, we therefore compare the results obtained by the following: Polarized SARA, Polarized SARA without constraint, TV problem with and without constraint, and ℓ_1 + TV problem with and without constraint. It is important to emphasize that all these problems are solved using primal–dual approaches. More specifically, while the first two problems are solved by Algorithm 2, which incorpo-

rates Algorithm 1 in each iteration, Algorithm 3 is used to solve the last four problems. These comparisons correspond to analysing not only the performance of different sparsifying regularizations for EHT imaging, but also the importance of polarization constraint for these regularizations.

In order to be coherent with the previous studies (Chael et al. 2016; Akiyama et al. 2017a,b) for EHT imaging, we also perform the comparison with the widely used Cotton–Schwab CLEAN (CS-CLEAN) algorithm (Schwab 1984). To this purpose, for each considered data set in this paper, we implemented CS-CLEAN in the Common Astronomy Software Applications (CASA) package[4].

5.5 Comparison in the super-resolution regime

Another comparison that can be made between the results obtained by different sparsifying regularizations is regarding the optimal resolution achieved by the respective reconstructed images, especially in the super-resolution regime, that is, when one goes beyond the nominal interferometric resolution (λ/B_{max}), also referred to as the diffraction limit. In this context, we adopt the comparison scheme introduced in Chael et al. (2016) and later used in Coughlan & Gabuzda (2016) and Akiyama et al. (2017a,b). It consists of convolving the reconstructed images with circular Gaussian beams of varying full width at half-maximum (FWHM) sizes. We then compute the normalized root mean square error (NRMSE) between these convolved images and the corresponding ground-truth images. It is to be mentioned that such a convolution varies the resolution of the underlying images. Therefore, not only the reconstruction errors, but also the errors due to loss of resolution will contribute to the computed NRMSEs. We compare the curves obtained from the TV problem with constraint, ℓ_1 + TV problem with constraint, Polarized SARA and CS-CLEAN. For the TV and ℓ_1 + TV problems with constraint, we consider the implementation of Algorithm 3. This already provides a better scenario for these TV-based regularizations, and hence accounts for a fair comparison of the performance of these methods with the Polarized SARA.

5.6 Simulation settings

For each of the cases discussed earlier, we perform five simulations varying the noise realizations. In order to stop the computation of the algorithm at convergence, we consider a stopping criterion.

First, we ensure that at convergence the residual norm is in the vicinity of the ℓ_2 upper bound ϵ defined in Section 5.1, i.e. $\|\Phi(\mathbf{S}) - \mathbf{Y}\|_2 \leq (1+\vartheta)\epsilon$, where $\vartheta > 0$ is a tolerance parameter. We set it equal to 5×10^{-3}. In addition, as the second stopping criterion, we impose the relative variation between two consecutive iterates to be very small, i.e.

$$\max_{i\in\{1,2,3\}} \left(\|\mathbf{S}_{:,i}^{(k+1)} - \mathbf{S}_{:,i}^{(k)}\|_2 / \|\mathbf{S}_{:,i}^{(k)}\|_2 \right) \leq \varepsilon, \tag{47}$$

where $\varepsilon > 0$. Concerning the case with the polarization constraint, not only the two above-mentioned criteria are taken into account, but we also verify that the constraint is satisfied, up to a small error, i.e. $N_p \leq \varrho$, where $\varrho > 0$.

As described previously, the proposed Polarized SARA method as well as the Polarized SARA without constraint method incorporate the reweighting scheme (Algorithm 2), wherein we perform 10 reweighting iterations. For each iteration and for both methods, we choose $\varepsilon = 10^{-5}$ in equation (47). In addition to this, we choose $\varrho = 0.5$ to stop Algorithm 1 for Polarized SARA. This choice of ϱ stops the algorithm when only 0.5 per cent of the pixels in the polarization error image, generated from the reconstructed Stokes images, are not satisfying the constraint (4).

Regarding the implementation of Algorithm 3 to solve for the TV and ℓ_1 + TV problems without constraint, we choose $\varepsilon = 10^{-5}$ for the forward-jet model, and 7×10^{-6} for the counter-jet model for the stopping criterion. While solving for the TV and ℓ_1 + TV problems with constraint, we also choose $\varrho = 0.5$. For the threshold parameters $\mathbf{\Lambda}$ in Algorithm 3, we tune these values to minimize the NRMSE. For any true image $\bar{s}$ and the corresponding reconstructed image $\boldsymbol{s}$, NRMSE is defined as

$$\text{NRMSE} = \sqrt{\frac{\sum_n |s_n - \bar{s}_n|^2}{\sum_n |\bar{s}_n|^2}}. \tag{48}$$

Therefore, with this definition, lower the NRMSE is, better the reconstruction is.

Table 1. SNR and NRMSE values for the reconstructed images corresponding to the (a) forward-jet model and (b) counter-jet model, obtained by different sparsifying regularizations. For each case, the mean values (computed over 5 simulations) are shown for the Stokes *I* image and the linear polarization image reconstructed with and without imposing the polarization constraint.

	Polarization constraint		
	TV	ℓ_1 + TV	SARA
(a) Forward-jet model			
Stokes *I* image (SNR/NRMSE)			
without constraint	27.53 / 0.2549	27.64 / 0.2542	33.09 / 0.1912
with constraint	28.19 / 0.2442	28.72 / 0.2378	33.15 / 0.1906
Linear polarization image (SNR/NRMSE)			
without constraint	23.66 / 0.3063	24.46 / 0.2944	27.54 / 0.2527
with constraint	24.92 / 0.2876	24.91 / 0.2878	28.96 / 0.2350
(b) Counter-jet model			
Stokes *I* image (SNR/NRMSE)			
without constraint	12.81 / 0.5269	12.82 / 0.5268	15.97 / 0.4502
with constraint	13.51 / 0.5089	13.51 / 0.5090	16.71 / 0.4337
Linear polarization image (SNR/NRMSE)			
without constraint	5.03 / 0.7781	5.85 / 0.7469	9.01 / 0.6374
with constraint	8.62 / 0.6500	8.77 / 0.6449	9.51 / 0.6215

5.7 Results and discussion

For a quantitative comparison between the reconstructed images from different cases, the reconstruction quality is assessed in terms of NRMSE as well as the signal-to-noise ratio (SNR). It is defined as

$$\text{SNR} = 20 \log_{10} \left(\frac{||\bar{\boldsymbol{s}}||_2}{\|\boldsymbol{s} - \bar{\boldsymbol{s}}\|_2} \right), \tag{49}$$

implying that higher SNR corresponds to better reconstruction quality. These NRMSE and SNR values for the reconstructed Stokes *I* image and the linear polarization image *P*, generated from the reconstructed Stokes *Q* and *U* images, are listed in Table 1 for both sets of models: the forward-jet model and the counter-jet model. In each case, the value shown corresponds to the mean value computed over the performed five simulations. It can be observed from Table1 that, on the one hand, for a given regularization, imposing

[4] https://casa.nrao.edu/

Table 2. Percentage of pixels not satisfying the polarization constraint in the reconstructed images obtained by without imposing the polarization constraint in the reconstruction process. The percentage is listed for the reconstructed images corresponding to the forward-jet model (first row), and the counter-jet model (second row). Each column represents the values corresponding to the reconstructed images obtained by different sparsifying regularizations. For each case, the values correspond to the mean values computed over five simulations.

Model	TV	ℓ_1 + TV	SARA
Forward-jet	20.47	16.14	15.02
Counter-jet	62.97	59.96	41.97

the polarization constraint yields lesser error (and thus higher SNR) in the reconstructions than that obtained without imposing it. More precisely, irrespective of the chosen regularization, enforcement of this constraint leads to improvement in the reconstruction quality. On the other hand, comparison between different regularizations shows that the SARA regularization performs significantly better than the other two regularizations, having a SNR ∼1–5 dBs higher. This holds true not only for Polarized SARA but also for Polarized SARA without constraint. This indicates the importance of choosing a suitable dictionary for better reconstruction. Concerning the importance of the polarization constraint, we quantify it by giving the percentage (N_p) of the pixels not fulfilling this constraint in Table 2. In particular, this table provides the values of N_p for cases in the absence of enforcement of the polarization constraint, whereas in its presence $N_p \leq 0.5$ per cent, as specified in the stopping criterion. Table 2 demonstrates that without imposing this constraint, an appreciable percentage of pixels have non-physical values. Additionally, in terms of the sparsifying regularizations, it again indicates the better performance of the SARA regularization in comparison with the others.

For the comparison in the super-resolution regime and as mentioned in Section 5.5, the NRMSE plots for both the forward-jet (first column) and counter-jet (second column) models are shown in Fig.3. The first and second rows, respectively, display the plots for the Stokes *I* and the linear polarization image *P*. In all these plots, the curve (solid thick, grey curve) labelled Model depicts the NRMSE values between the ground-truth images convolved with circular Gaussian beams of varying FWHM sizes and the original ground-truth images. Relating this to the previous discussion (Section 5.5), this curve basically represents the minimum attainable errors at any given resolution, arising purely because of the loss of resolution. The other curves correspond to the following: TV problem with constraint (dotted red curve), ℓ_1 + TV problem with constraint (dash-dotted green curve) and Polarized SARA (dashed blue curve). We also give the curve (solid thin, pink curve) obtained by the reconstructions from the widely used CS-CLEAN algorithm (Schwab 1984) using uniform weighting.

It can be seen that for the Stokes *I* images, CS-CLEAN NRMSE values start to increase rapidly in the super-resolution regime, where the diffraction limit is specified by the FWHM of size 1. This indicates the inability of CS-CLEAN to produce super-resolved images. Moreover, in this case, the minimum errors are obtained at a resolution of ∼50–80 per cent of the diffraction limit. On the contrary, for the other considered sparsifying regularizations, the NRMSE values vary gradually even in the super-resolution regime. In fact, the error tends to decrease. It can be noticed that the values for the TV and ℓ_1 + TV problems with constraint are quite close, whereas the errors from the Polarized SARA are less than those obtained by the former two. Another interesting observation is related to the resolution where the minimum error is achieved by these regularizations. While for the TV and ℓ_1 + TV problems, it is at ∼25–35 per cent of the diffraction limit, the corresponding value for the Polarized SARA is 0 per cent. This highlights that the reconstructions obtained by the latter do not need to be convolved with a restoring beam. This is in contrast to the results obtained by other curves, where convolution with a restoring beam is required to obtain the minimum error. The same features are noticed from the plots of the linear polarization images. In this case, the errors obtained by CS-CLEAN are quite large, with the minimum being at around 60 per cent of the interferometric resolution. These large errors indicate that CS-CLEAN is not particularly suitable for recovering the linearly polarized emission images.

For visual comparison of the results obtained from these tests, we show the reconstructed images and the respective error images. The latter are computed by taking the absolute difference between the true and the reconstructed images. Out of the five simulations, the displayed images correspond to the simulation results with the least NRMSE. The results for the forward-jet model images are shown in Figs 4 and 5, respectively, for the intensity image *I* and the linear polarization image *P*. In both figures, the first row shows the ground-truth image, whereas the second row shows the CS-CLEAN reconstruction followed by its error image. For the CS-CLEAN reconstruction, the image corresponds to the model image convolved with the restoring beam of FWHM size giving the minimum error for this method. Third and fourth rows show the results for the TV and ℓ_1 + TV problems, respectively. In these rows, while the first two columns show the reconstructed and the error images obtained without imposing the polarization constraint in the reconstruction process, the respective images obtained in the presence of the constraint are shown in the last two columns. Similarly, for the last row, column-wise, the following are displayed: reconstructed image for Polarized SARA without constraint and its error image; reconstructed image for Polarized SARA and its error image. In the same manner, the results for the intensity image and the linear polarization image for the counter-jet model are shown in Figs 6 and 7, respectively.

Comparing the different regularizations from these figures, we can observe that the reconstructions obtained using the TV and ℓ_1 + TV regularizations are similar, while employing the SARA regularization leads to a better reconstruction quality. First, in the case of the intensity image, for both forward and counter-jet models, the central region is much more resolved for the SARA regularization. This contrasts with the reconstructions obtained by the TV and ℓ_1 + TV regularizations, where only the sharp edges are retained, leading to the staircase effect. We can recall that this effect arises due to the definition of the TV regularization, which tends to promote piece-wise constant images. Secondly, for the linear polarization images, while all the regularizations produce diffused emissions in the background, these artefacts in the background are lower in the case of SARA regularization. In particular for the counter-jet model, the SARA regularization performs significantly better than the other two. It is to be noted that with the same noise variance, the low-intensity values of this model provides less SNR than the forward-jet model images. Thus, the image reconstruction is much more challenging in this case. The superiority of the SARA regularization over other regularizations in reconstructing these images is also supported by the error images. All these images are shown in the linear scale, and we can see that for the

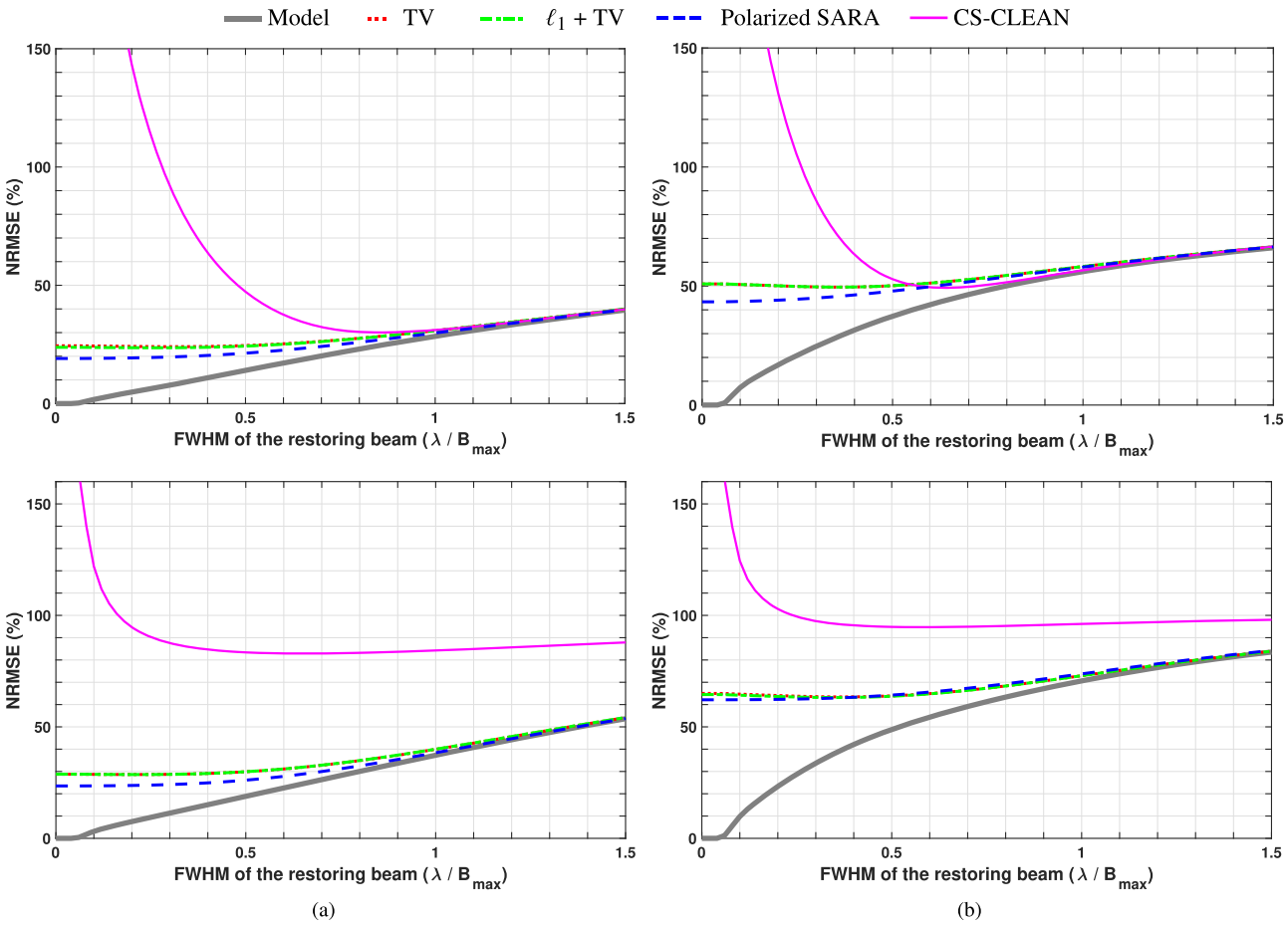

Figure 3. The NRMSE plots for the Stokes *I* image (first row) and the linear polarization image (second row) corresponding to (a) the forward-jet model and (b) the counter-jet model, as a function of the FWHM size of the restoring beam. The NRMSE is evaluated between the original ground-truth image and the beam-convolved reconstructed images. Different curves represent the errors for different regularizations while incorporating the polarization constraint: TV problem with constraint (dotted red curve), ℓ_1 + TV problem with constraint (dash-dotted green curve) and Polarized SARA (dashed blue curve). While the pink curve (solid thin curve) corresponds to the reconstructions obtained by CS-CLEAN, the grey curve (solid thick curve) shows the errors for the Model (i.e. the error between the original ground-truth image and the beam-convolved ground-truth image).

TV and ℓ_1 + TV regularizations, these images have more residual, especially in the background. Furthermore, for the CS-CLEAN reconstructions, it can be observed that the reconstruction quality is worse than that obtained using any other sparsifying regularization, especially for the linear polarization image, validating the high errors observed in Fig.3. These observations are consistent with those obtained in other studies (Chael et al. 2016; Akiyama et al. 2017a,b).

Regarding the comparison between the cases with and without polarization constraint, reduction in the artificial diffused background emissions, especially for the linear polarization images, by enforcing the constraint can be noticed from the presented results. This is supported by the visual inspection of the results as well as by the lesser residual in the error images. In particular for linear polarization images of counter-jet model, there is an appreciable improvement in the reconstruction quality for the TV and ℓ_1 + TV regularizations.

The results show the suitability of the SARA regularization for EHT imaging. Moreover, the use of the polarization constraint not only imposes the physical coherency between the reconstructed images, but it also tends to improve the reconstruction quality, independent of the choice of the sparsifying regularization. The latter is even more evident in the reconstruction of the the images with low SNR, as observed for the linear polarization images for the counter-jet model. Furthermore, it is to be noted that the non-physical reconstructions obtained in the absence of the constraint are more likely to appear in the background where the total intensity image has smaller values. To illustrate this assertion, the corresponding polarization error images are presented in Fig.8 for the forward- and counter-jet models, respectively, in the first and second columns. As previously mentioned, these images basically show the pixels where the polarization constraint is not satisfied by the reconstructed Stokes images. Having only 0.5 per cent (corresponding to the chosen stopping criterion) of such undesirable pixels, we do not show the polarization error images obtained in the presence of the constraint. In Fig.8, the images are shown for the following: TV problem without constraint (first row), ℓ_1 + TV problem without constraint (second row) and Polarized SARA without constraint (third row). It can be clearly seen from these images that not imposing the constraint leads to the reconstruction of many pixels with physically unacceptable values. Another observation is regarding the SARA regularization, which performs better in suppressing these pixels than the other two regularizations, coherent with the values in Table 2.

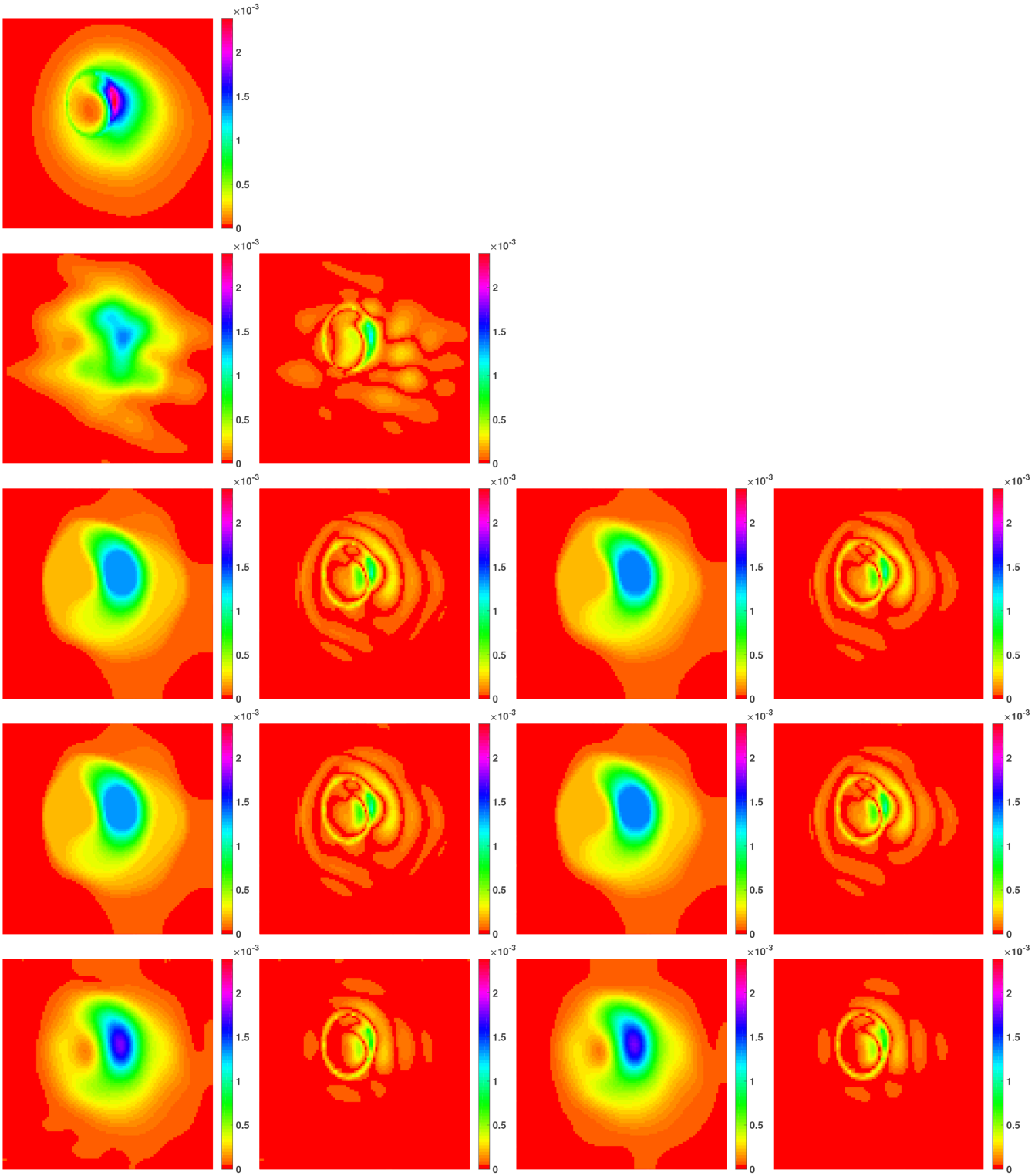

Figure 4. Results for the Stokes *I* image corresponding to the forward-jet model. The first row shows the ground-truth image, whereas the second row shows the CS-CLEAN reconstructed image followed by its error image. The third and fourth rows show the results for the TV and ℓ_1 + TV problems, respectively. For these rows, the first two columns show the reconstructed and the error images obtained without imposing the polarization constraint in the reconstruction process, whereas the corresponding images in the case of imposing this constraint are shown in the last two columns. Similarly, column-wise, the last row displays the reconstructed image for Polarized SARA without constraint and its error image, and the reconstructed image for Polarized SARA and its error image. The images correspond to the best results obtained over five performed simulations for each case. All the images are shown in linear scale, normalized to the scale of the corresponding ground-truth image.

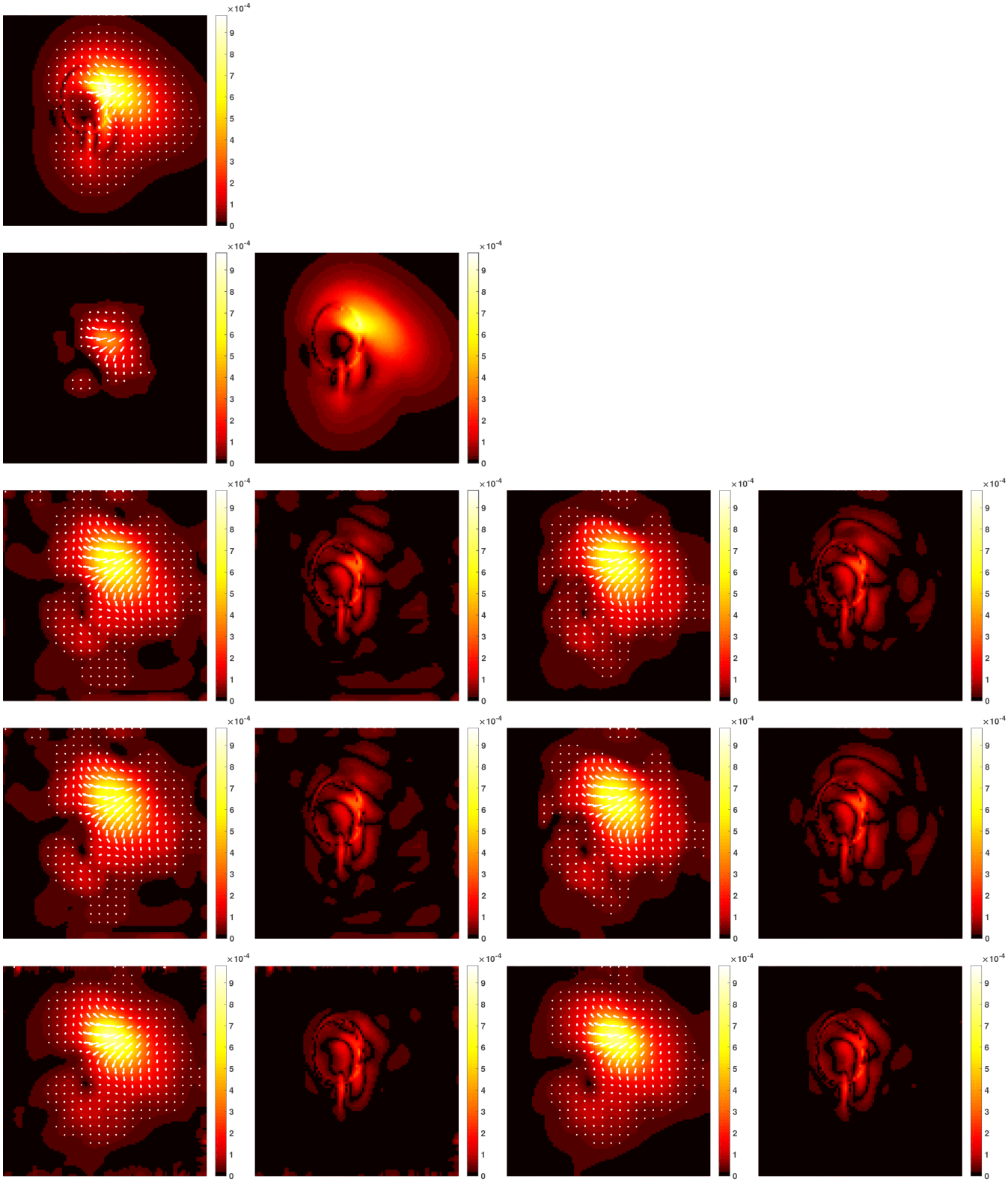

Figure 5. Results for the linear polarization image corresponding to the forward-jet model. The first row shows the ground-truth image, whereas the second row shows the CS-CLEAN reconstructed image followed by its error image. The third and fourth rows show the results for the TV and ℓ_1 + TV problems, respectively. For these rows, the first two columns show the reconstructed and the error images obtained without imposing the polarization constraint in the reconstruction process, whereas the corresponding images in the case of imposing this constraint are shown in the last two columns. Similarly, column-wise, the last row displays the reconstructed image for Polarized SARA without constraint and its error image, and the reconstructed image for Polarized SARA and its error image. The shown images are the linear polarization intensity images, overlaid by the white bars representing the EVPA. These images correspond to the best results obtained over five performed simulations for each case. All the images are shown in linear scale, normalized to the scale of the corresponding ground-truth image.

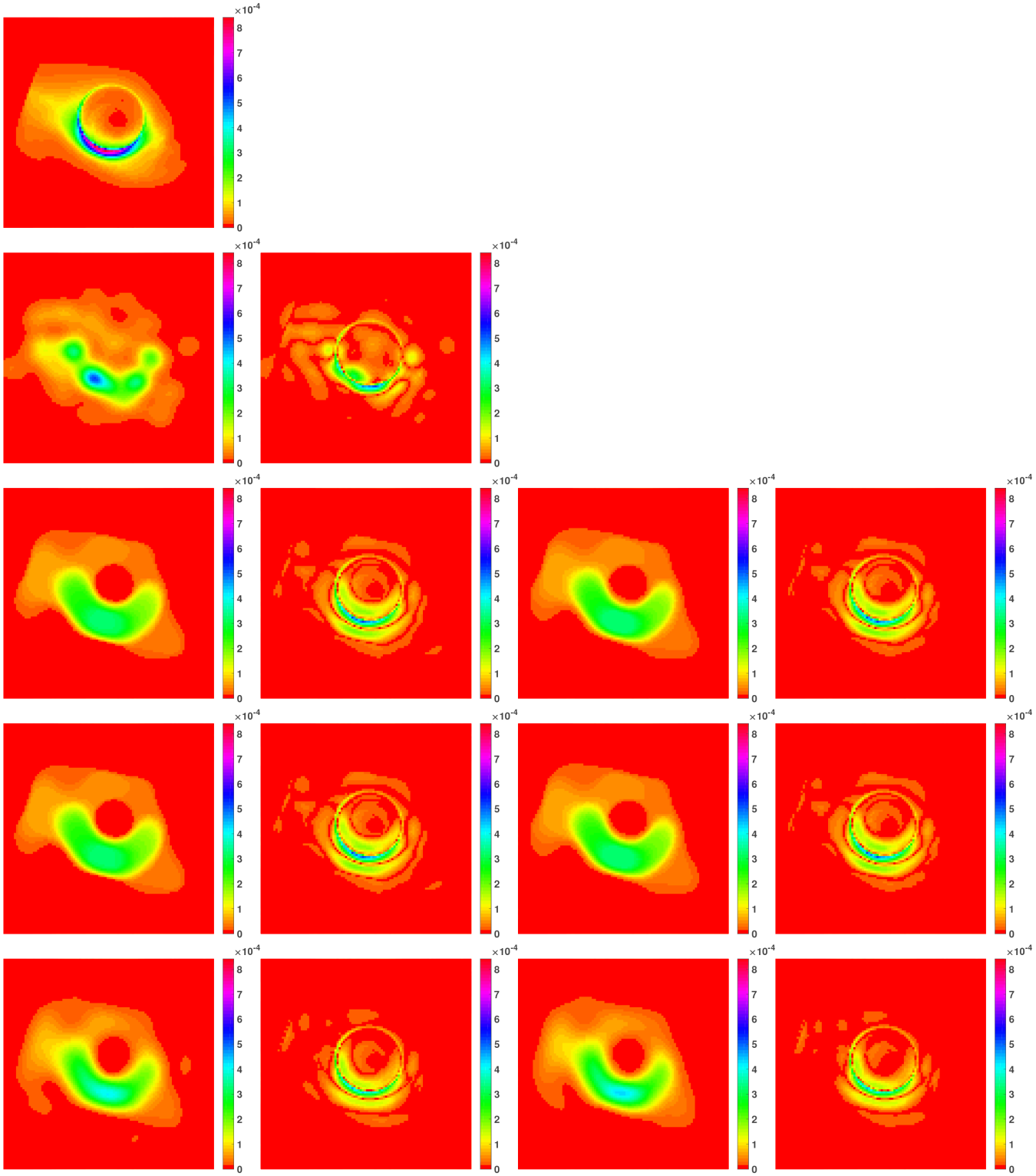

Figure 6. Results for the Stokes *I* image corresponding to the counter-jet model. The first row shows the ground-truth image, whereas the second row shows the CS-CLEAN reconstructed image followed by its error image. The third and fourth rows show the results for the TV and ℓ_1 + TV problems, respectively. For these rows, the first two columns show the reconstructed and the error images obtained without imposing the polarization constraint in the reconstruction process, whereas the corresponding images in the case of imposing this constraint are shown in the last two columns. Similarly, column-wise, the last row displays the reconstructed image for Polarized SARA without constraint and its error image, and the reconstructed image for Polarized SARA and its error image. The images correspond to the best results obtained over five performed simulations for each case. All the images are shown in linear scale, normalized to the scale of the corresponding ground-truth image.

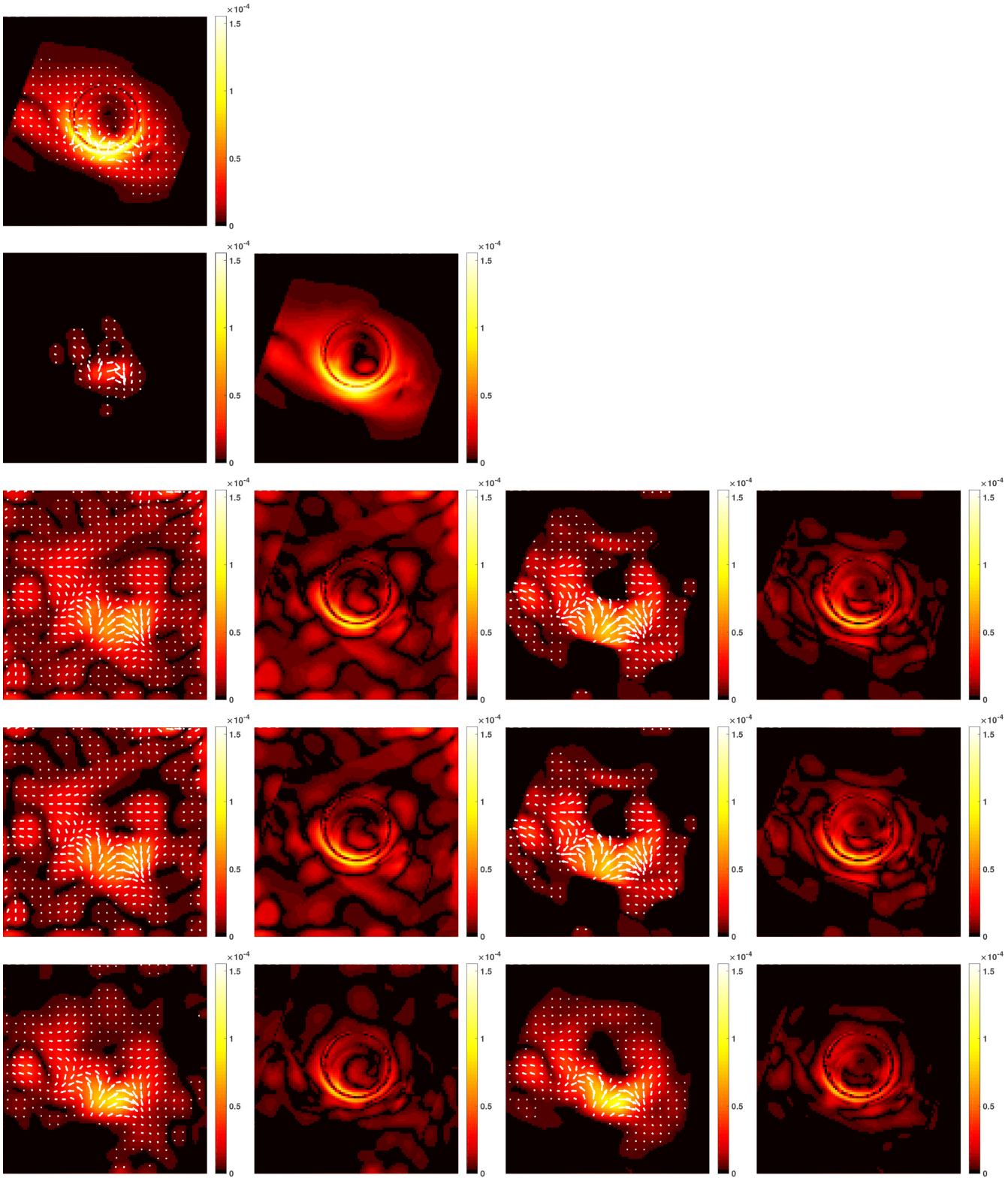

Figure 7. Results for the linear polarization image corresponding to the counter-jet model. The first row shows the ground-truth image, whereas the second row shows the CS-CLEAN reconstructed image followed by its error image. The third and fourth rows show the results for the TV and ℓ_1 + TV problems, respectively. For these rows, the first two columns show the reconstructed and the error images obtained without imposing the polarization constraint in the reconstruction process, whereas the corresponding images in the case of imposing this constraint are shown in the last two columns. Similarly, column-wise, the last row displays the reconstructed image for Polarized SARA without constraint and its error image, and the reconstructed image for Polarized SARA and its error image. The shown images are the linear polarization intensity images, overlaid by the white bars representing the EVPA. These images correspond to the best results obtained over five performed simulations for each case. All the images are shown in linear scale, normalized to the scale of the corresponding ground-truth image.

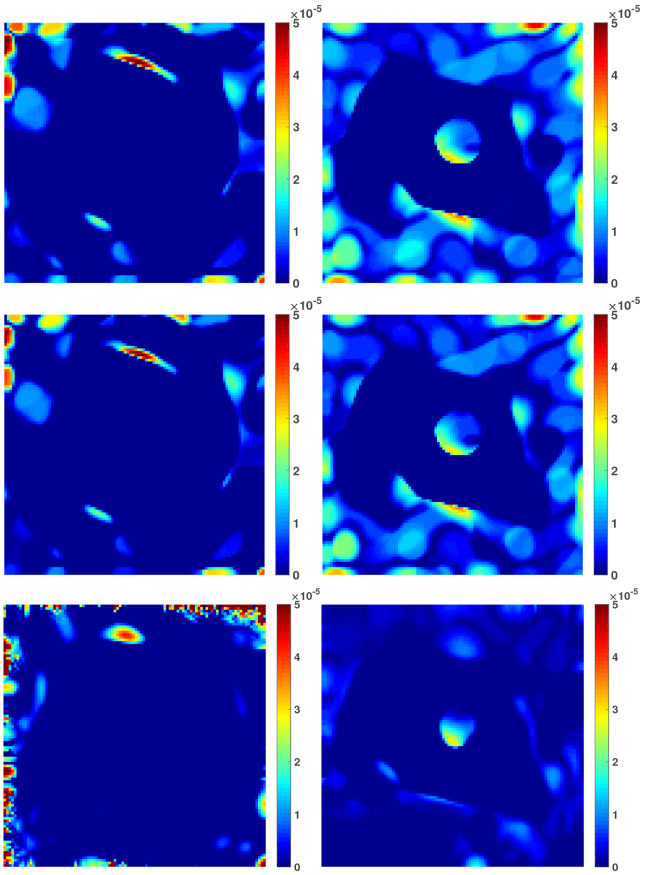

Figure 8. The polarization error images for the forward-jet model (first column) and the counter-jet model (second column) showing the pixels where the polarization constraint is not satisfied. These images are computed from the reconstructions obtained from the TV problem without constraint (first row), ℓ_1 + TV problem without constraint (second row) and Polarized SARA without constraint (third row). All the images are shown in linear scale. It is to be mentioned here that in the case of imposing this constraint, the corresponding polarization error images only have around 0.5 per cent non-zero pixels, as ensured in the stopping criterion.

6 CONCLUSION AND DISCUSSION

We have presented a new method, called Polarized SARA, for joint estimation of sparse Stokes images in the context of radio interferometry (RI), considering explicitly the polarization constraint. The latter is used to exploit the physical link between the Stokes images, imposing the polarization intensity as a lower bound on the total intensity image. We have proposed to deal with this constraint using the techniques of epigraphical projection, solving for a convex optimization problem. In addition, our method leverages the sparsity of the underlying images using SARA regularization which consists in promoting the average sparsity of each Stokes parameter using the weighted ℓ_1 norm encompassed in a reweighted scheme. Thanks to this weighting, the proposed method does not require the tuning of any regularization parameter and only the noise bound needs to be specified. To solve the resultant image reconstruction problem, we have designed an iterative proximal primal–dual algorithm. In this respect, the proposed approach presents the first application of sparsity based optimization techniques for the reconstruction of Stokes images, taking into account the polarization constraint within a convex formulation. Moreover, our algorithm presents a highly versatile structure. This allows the incorporation of different sparsifying regularizations in the algorithm. The MATLAB code of the proposed method is available on GitHub (https://basp-group.github.io/stokes-imaging/).

We have applied the proposed Polarized SARA method to the simulated EHT data sets. For the choice of sparsifying regularization, apart from the SARA regularization, we have also considered the TV and ℓ_1 + TV regularizations, the latter two being suggested in Akiyama et al. (2017a) for full-polarization EHT imaging. To judge the effect of the polarization constraint on the reconstruction quality, we have also generalized the problem considered in Akiyama et al. (2017a) to take into account this constraint. It is solved using a modified version of the proposed algorithm. It is to be noted that this generalization provides an improvement over the technique used in Akiyama et al. (2017a), because of its scalability, non-sub-iterative nature (especially for the ℓ_1 + TV regularized problem) as well as the incorporation of the polarization constraint. On the one hand, the comparison between the different cases considered indicates the importance of imposing the polarization constraint in reconstructing physically acceptable images. Additionally, irrespective of the considered sparsifying regularization, the enforcement of this constraint tends to enhance the reconstruction quality, particularly for the linear polarization images. This enhancement is significant for the results obtained by solving the TV and ℓ_1 + TV problems with constraint. Thus, we can conclude that the polarization constraint is highly effective in producing images not only with physical meaning, but also with fewer artefacts.

On the other hand, regarding the choice of sparsifying regularization, the results demonstrate the ability of the SARA regularization to produce images with better reconstruction quality and higher resolution, without requiring the convolution of the reconstructed images with any restoring beam. First, for Stokes *I* imaging, for which this regularization was initially proposed, its good performance is in agreement with the previous studies (Carrillo et al. 2012, 2014; Onose et al. 2017). These reconstructions also prevail over those obtained by the standard CS-CLEAN algorithm. Secondly, the obtained results also highlight the suitability of SARA regularization for polarimetric imaging. Indeed, Polarized SARA yields better results for the considered data sets than solving the TV-based problems, both with and without the constraint. Thus, the proposed Polarized SARA method stands out as a promising candidate for polarimetric imaging in RI. Moreover, its scalable version is developed in Birdi et al. (2018), exploiting the distribution and parallelization capabilities of the underlying primal–dual framework to handle large-scale data sets.

It is worth emphasizing again that the proposed approach has been developed to solve for the general RIME formalism (1). However, in the current simulation settings, we have dealt with the case when the calibration terms, DIEs and DDEs, are absent. For future work, we plan to consider the general setting of RIME, which essentially consists in adapting the measurement operator to take into account these terms. In such a case, with known DIEs and DDEs, the problem of reconstructing the Stokes images can be solved by employing a similar approach as the one described in this paper. Furthermore, the more challenging case of unknown calibration terms can be tackled using the ideas from our previous work on joint calibration and imaging for Stokes *I* (Repetti et al. 2017).

Additionally, in the context of linear polarimetric imaging, a potential future prospect is to reconstruct the Stokes *I* image with the linear polarization image *P* directly, instead of obtaining the image *P* from the estimations of Stokes *Q* and *U*. This stems from the fact that the magnitudes of the latter two can vary depending on the orientation of the chosen coordinate system, whereas the magnitude

of the linear polarization image is independent of the choice of the coordinate system. Moreover, the problem can be solved for the rotationally invariant electric and magnetic components, defined from Stokes Q and U parameters (Wiaux, Jacques & Vandergheynst 2007). We also note that while the current approach deals with the complex visibilities, an interesting extension would be to apply it on VLBI observations, where the visibility phase information cannot be acquired. In this case, as mentioned earlier, we can work either with the self-calibrated data or in conjuction with sparsity-based optical interferometric techniques (Birdi et al. 2017).

Our work can also be directly adapted to hyperspectral imaging as the polarization constraint acts at each wavelength independently. More complex priors can obviously be incorporated into the associated minimization problem, in line with recent results by one of the authors (Abdulaziz et al. 2016). Such developments are of critical interest for Faraday synthesis (Brentjens & De Bruyn 2005; Bell & Enßlin 2012).

ACKNOWLEDGEMENTS

This work was supported by the UK Engineering and Physical Sciences Research Council (EPSRC, grant EP/M011089/1).

REFERENCES

Abdulaziz A., Dabbech A., Onose A., Wiaux Y., 2016, in Proc. EUSIPCO. IEEE, Conference location: Budapest, Hungary, p. 388
Akiyama K. et al., 2015, ApJ, 807, 150
Akiyama K. et al., 2017a, AJ, 153, 159
Akiyama K. et al., 2017b, ApJ, 838, 1
Bauschke H. H., Combettes P. L., 2011, Convex Analysis and Monotone Operator Theory in Hilbert Spaces. Springer, New York
Beck A., Teboulle M., 2009a, J. Imaging Sci., 2, 183
Beck A., Teboulle M., 2009b, IEEE Trans. Image Process., 18, 2419
Bell M. R., Enßlin T., 2012, A&A, 540, A80
Bhatnagar S., Cornwell T. J., 2004, A&A, 426, 747
Birdi J., Repetti A., Wiaux Y., 2017, MNRAS, 468, 1142
Birdi J., Repetti A., Wiaux Y., 2018, Proc. IEEE SAM, in press
Brentjens M., De Bruyn A., 2005, A&A, 441, 1217
Broderick A., Loeb A., 2009, ApJ, 697, 1164
Candès E., Romberg J., Tao T., 2006, IEEE Trans. Inf. Theory, 52, 489
Candès E., Wakin M., Boyd S., 2008, J. Fourier Anal. Appl., 14, 877
Carrillo R., McEwen J., Wiaux Y., 2012, MNRAS, 426, 1223
Carrillo R., McEwen J., Van De Ville D., Thiran J.-P., Wiaux Y., 2013, IEEE Signal Process. Lett., 20, 591
Carrillo R., McEwen J., Wiaux Y., 2014, MNRAS, 439, 3591
Chael A., Johnson M., Narayan R., Doeleman S., Wardle J., Bouman K., 2016, AJ, 829, 11
Chambolle A., Lions P., 1997, Numerische Mathematik, 76, 167
Chambolle A., Pock T., 2010, J. Math. Imag. Vision, 40, 120
Chaux C., Combettes P. L., Pesquet J.-C., Wajs V. R., 2007, Inverse Problems, 23, 1495
Chen G., Rockafellar R., 1997, SIAM J. Optim., 7, 421
Chen S. S., Donoho D. L., Saunders M. A., 2001, SIAM Rev., 43, 129
Chierchia G., Pustelnik N., Pesquet J.-C., Pesquet-Popescu B., 2014, in 2014 IEEE International Conference on Acoustics, Speech and Signal Processing (ICASSP). IEEE, Piscataway, NJ, p. 8312
Chierchia G., Pustelnik N., Pesquet J.-C., Pesquet-Popescu B., 2015, Sig. Image Vid. Process., 9, 1737
Combettes P. L., Pesquet J.-C., 2011, Fixed-Point Algorithms for Inverse Problems in Science and Engineering. Springer, New York
Combettes P. L., Condat L., Pesquet J.-C., Vũ B., 2014, in 2014 IEEE International Conference on Image Processing (ICIP). IEEE, Piscataway, NJ, p. 4141
Condat L., 2013, J. Opt. Theory Appl., 158, 460
Cornwell T. J., 2008, IEEE J. Sel. Top. Sig. Process., 2, 793
Cornwell T. J., Evans K. F., 1985, A&A, 143, 77
Cornwell T. J., Golap K., Bhatnagar S., 2008, IEEE J. Sel. Top. Sig. Process., 2, 647
Coughlan C., Gabuzda D., 2016, MNRAS, 463, 1980
Dabbech A., Onose A., Abdulaziz A., Perley R., Smirnov O., Wiaux Y., 2017a, MNRAS, 476, 2853
Dabbech A., Wolz L., Pratley L., McEwen J., Wiaux Y., 2017b, MNRAS, 471, 4300
Daubechies I., Sweldens W., 1998, J. Fourier Anal. Appl., 4, 247
Dexter J., 2016, MNRAS, 462, 115
Dexter J., McKinney J., Agol E., 2012, MNRAS, 421, 1517
Doeleman S. et al., 2008, Nature, 455, 78
Doeleman S. et al., 2012, Science, 338, 355
Donoho D. L., 2006, IEEE Trans. Inf. Theory, 52, 1289
Donoho D., Johnstone I., Kerkyacharian G., Picard D., 1995, J. R. Stat. Soc. Ser. B, 57, 301
Dreher J., Carilli C., Perley R., 1987, ApJ, 316, 611
Eckstein J., Bertsekas D., 1992, Math. Program., 55, 293
El-Gheche M., Chierchia G., Pesquet J.-C., 2016, p reprint (arXiv:1606.09552)
Fessler J. A., Sutton B. P., 2003, IEEE Trans. Signal Process., 51, 560
Garsden H. et al., 2015, A&A, 575, A90
Ginzburg V., Syrovatskii S., 1965, ARA&A, 3, 297
Hamaker J., Bregman J., Sault R., 1996, A&AS, 117, 137
Harizanov S., Pesquet J.-C., Steidl G., 2013, in Proc. Int. Conf. on Scale Space and Variational Methods in Computer Vision. Springer, Berlin, p. 125
Högbom J. A., 1974, A&A, 15, 417
Holdaway M., Wardle J., 1990, Digital Image Synthesis and Inverse Optics, 1351, 714
Komodakis N., Pesquet J.-C., 2015, IEEE Sig. Proc. Mag., 32, 31
Li F., Cornwell T., De hoog F., 2011, A&A, 528, A31
Lu R., Broderick A., Baron F., Monnier J., Fish V., Doeleman S., Pankratius V., 2014, ApJ, 788, 120
Mallat S. G., 2009, A Wavelet Tour of Signal Processing: The Sparse Way, 2nd edn. Academic Press, Burlington, MA
Mallat S., Zhang Z., 1993, IEEE Trans. Signal Process., 41, 3397
Moerkotte G., Montag M., Repetti A., Steidl G., 2015, J. Comp. App. Math., 285, 243
Narayan R., Nityananda R., 1986, ARA&A, 24, 127
Offringa A. et al., 2014, MNRAS, 444, 606
Onose A., Carrillo R., Repetti A., McEwen J., Thiran J., Pesquet J.-C., Wiaux Y., 2016, MNRAS, 462, 4314
Onose A., Dabbech A., Wiaux Y., 2017, MNRAS, 469, 938
Pacholczyk A., 1970, Radio Astrophysics: Nonthermal Processes in Galactic and Extragalactic Sources. Freema and co, San Francisco
Pesquet J.-C., Repetti A., 2015, J. Nonlinear Convex Anal., 16, 2453
Pratley L., Johnston-Hollitt M., 2016, MNRAS, 462, 3483
Pratley L., McEwen J., d'Avezac M., Carrillo R., Onose A., Wiaux Y., 2018, MNRAS, 473, 1038
Rau U., Bhatnagar S., Voronkov M., Cornwell T., 2009, Proc. IEEE, 97, 1472
Repetti A., Birdi J., Dabbech A., Wiaux Y., 2017, MNRAS, 470, 3981
Roberts D., Wardle J., Brown L., 1994, ApJ, 427, 718
Rockafellar R. T., Wets R. J.-B., 1997, Variational Analysis, 1st edn. Vol. 317. Springer, New York
Rubinstein R., Bruckstein A., Elad M., 2010,Proc. IEEE, 1045
Rudin L., Osher S., Fatemi E., 1992, Phys. D: Nonlinear Phenomena, 60, 259
Salvini S., Wijnholds S., 2014, A&A, 571, A97
Schwab F., 1984, AJ, 89, 1076
Simard-Normandin M., Kronberg P., Button S., 1981, ApJS, 45, 97
Smirnov O., 2011, A&A, 527, A107
Smirnov O., Tasse C., 2015, MNRAS, 449, 2668
Sokolowski M. et al., 2017, PASA, 34, e062

Starck J.-L., Murtagh F., Fadili J., 2010, Sparse Image and Signal Processing : Wavelets, Curvelets, Morphological Diversity. Cambridge Univ. Press, Cambridge
Thiébaut E., Giovannelli J., 2010, IEEE Signal Process. Mag., 27, 97
Thompson A., Moran J., Swenson G., 2001, Interferometry and Synthesis in Radio Astronomy. Wiley-Interscience, New York
Tseng P., 2000, SIAM J. Control Optim., 38, 431
Van Weeren R. et al., 2016, ApJS, 223, 2
Vũ B., 2013, Adv. Comp. Math., 38, 667
Wiaux Y., Jacques L., Vandergheynst P., 2007, J. Comp. Phys., 226, 2359
Wiaux Y., Jacques L., Puy G., Scaife A., Vandergheynst P., 2009, MNRAS, 395, 1733
Wiaux Y., Puy G., Vandergheynst P., 2010, MNRAS, 402, 2626

This paper has been typeset from a TEX/LATEX file prepared by the author.